



Identification and selection rules of the spin-wave eigen-modes in a normally magnetized nano-pillar

Vladimir V. Naletov, Grégoire De Loubens, Gonçalo Albuquerque, Simone Borlenghi, Vincent Cros, Giancarlo Faini, Julie Grollier, Hervé Hurdequint, Nicolas Locatelli, Benjamin Pigeau, et al.

► To cite this version:

Vladimir V. Naletov, Grégoire De Loubens, Gonçalo Albuquerque, Simone Borlenghi, Vincent Cros, et al.. Identification and selection rules of the spin-wave eigen-modes in a normally magnetized nano-pillar. *Physical Review B : Condensed matter and materials physics*, American Physical Society, 2011, 84 (22), pp.224423. <10.1103/PhysRevB.84.224423>. <hal-00610637v2>

HAL Id: hal-00610637

<https://hal.archives-ouvertes.fr/hal-00610637v2>

Submitted on 24 Oct 2011

HAL is a multi-disciplinary open access archive for the deposit and dissemination of scientific research documents, whether they are published or not. The documents may come from teaching and research institutions in France or abroad, or from public or private research centers.

L'archive ouverte pluridisciplinaire **HAL**, est destinée au dépôt et à la diffusion de documents scientifiques de niveau recherche, publiés ou non, émanant des établissements d'enseignement et de recherche français ou étrangers, des laboratoires publics ou privés.

Identification and selection rules of the spin-wave eigen-modes in a normally magnetized nano-pillar

V.V. Naletov,^{1,2} G. de Loubens,^{1,*} G. Albuquerque,³ S. Borlenghi,¹ V. Cros,⁴ G. Faini,⁵ J. Grollier,⁴ H. Hurdequint,⁶ N. Locatelli,⁴ B. Pigeau,¹ A. N. Slavin,⁷ V. S. Tiberkevich,⁷ C. Ulysse,⁵ T. Valet,³ and O. Klein^{1,†}

¹*Service de Physique de l'État Condensé (CNRS URA 2464), CEA Saclay, 91191 Gif-sur-Yvette, France*

²*Physics Department, Kazan Federal University, Kazan 420008, Russian Federation*

³*In Silicio, 730 rue René Descartes 13857 Aix En Provence, France*

⁴*Unité Mixte de Physique CNRS/Thales and Université Paris Sud 11, RD 128, 91767 Palaiseau, France*

⁵*Laboratoire de Photonique et de Nanostructures, Route de Nozay 91460 Marcoussis, France*

⁶*Laboratoire de Physique des Solides, Université Paris-Sud, 91405 Orsay, France*

⁷*Department of Physics, Oakland University, Michigan 48309, USA*

(Dated: October 24, 2011)

We report on a spectroscopic study of the spin-wave eigen-modes inside an individual normally magnetized two layers circular nano-pillar (Permalloy|Copper|Permalloy) by means of a Magnetic Resonance Force Microscope (MRFM). We demonstrate that the observed spin-wave spectrum critically depends on the method of excitation. While the spatially uniform radio-frequency (RF) magnetic field excites only the axially symmetric modes having azimuthal index $\ell = 0$, the RF current flowing through the nano-pillar, creating a circular RF Oersted field, excites only the modes having azimuthal index $\ell = +1$. Breaking the axial symmetry of the nano-pillar, either by tilting the bias magnetic field or by making the pillar shape elliptical, mixes different ℓ -index symmetries, which can be excited simultaneously by the RF current. Experimental spectra are compared to theoretical prediction using both analytical and numerical calculations. An analysis of the influence of the static and dynamic dipolar coupling between the nano-pillar magnetic layers on the mode spectrum is performed.

I. INTRODUCTION

Technological progress in the fabrication of hybrid nanostructures using magnetic metals has allowed the emergence of a new science aimed at utilizing spin dependent effects in the electronic transport properties¹. An elementary device of spintronics consists of two magnetic layers separated by a normal layer. It exhibits the well-known giant magneto-resistance (GMR) effect^{2,3}, that is, its resistance depends on the relative angle between the magnetic layers. Nowadays, this useful property is extensively used in magnetic sensors^{4,5}. The converse effect is that a direct current can transfer spin angular momentum between two magnetic layers separated by either a normal metal or a thin insulating layer^{6,7}. As a result, a spin polarized current leads to a very efficient destabilization of the orientation of a magnetic moment⁸. Practical applications are the possibility to control the digital information in magnetic random access memories (MRAMs)^{9,10} or to produce high frequency signals in spin transfer nano-oscillators (STNOs)^{11,12}.

From an experimental point of view, the precise identification of the spin-wave (SW) eigen-modes in hybrid magnetic nanostructures remains to be done¹³⁻¹⁸. Of particular interest is the exact nature of the modes excited by a current perpendicular-to-plane in STNOs. Here, the identification of the associated symmetry behind each mode is essential. It gives a fundamental insight about their selection rules and about the mutual coupling mechanisms that might exist intra or inter STNOs. It also determines the optimum strategy to couple to the auto-oscillating mode observed when the

spin transfer torque compensates the damping, a vital knowledge to achieve phase synchronization in arrays of nano-pillars¹⁹. These SW modes also have a fundamental influence on the high frequency properties of these devices and in particular on the noise of magneto-resistive sensors^{20,21}.

A natural mean to probe SW modes in hybrid nanostructures is to use their magneto-resistance properties. For instance, thermal SW can be directly detected in the noise spectrum of tunneling magneto-resistance (TMR) devices owing to their large TMR ratio^{22,23}. It is also possible to use spin torque driven ferromagnetic resonance (ST-FMR)²⁴⁻³⁰. In this approach, an RF current flowing through the magneto-resistive device is used to excite the precession of magnetization and to detect it through a rectification effect. Direct excitation of SW modes by the RF field generated by micro-antennas and their detection through dc rectification³¹ or high-frequency GMR measurements³² has also been reported in spin-valve sensors. In all these experiments, the static magnetizations in the spin-valve have to be misaligned in order for the magnetization precession to produce a finite voltage. Because highly symmetric magnetization trajectories do not produce any variation of resistance with time in some cases, a third magnetic layer playing the role of an analyzer can be introduced³³. In ST-FMR, the non-collinearity of the magnetizations is also required for the RF spin transfer excitation not to vanish^{25,26}. Moreover, the latter was never directly compared to standard FMR, where a uniform RF magnetic field is used to excite SW modes. Thus, although the voltage detection of SW eigen-modes in hybrid nanostructures is elegant, one

should keep in mind that some of them might be hidden due to symmetry reasons.

Here, we propose an independent method of detecting the magnetic resonance inside a spin-valve nanostructure. We shall use a Magnetic Resonance Force Microscope (MRFM)^{34–38}. A first decisive advantage of the MRFM technique is that the detection scheme does not rely on the SW spatial symmetry because it measures the change in the longitudinal component of the magnetization. Like a bolometric detection, mechanical based FMR detects *all* the excited SW modes, independently of their phase^{39,40}. A second decisive advantage is that MRFM is a very sensitive technique that can measure the magnetization dynamics in nanostructures buried under metallic electrodes^{41–43}. Indeed, the probe is a magnetic particle attached at the end of a soft cantilever and is coupled to the sample through the dipolar interaction.

In our roadmap to characterize the nature of the auto-oscillation modes in STNOs, we report in this work on a comprehensive identification of the SW eigen-modes in the simplest possible geometry: the normally magnetized circular spin-valve nano-pillar. This configuration is obtained by saturating the device with a large external magnetic field oriented perpendicular to the layers. Thanks to the preserved axial symmetry, a simplified spectroscopic signature of the different SW eigen-modes is expected. This identification is achieved experimentally from a comparative spectroscopic study of the SW eigen-modes excited either by an RF current flowing perpendicularly through the nano-pillar, as used in ST-FMR, or by a homogeneous RF in-plane magnetic field, as used in conventional FMR. It shall be developed as follows. In section II, we present the MRFM setup and the experimental protocol used to perform SW spectroscopy in a spin-valve. We show that the SW spectrum excited by a homogeneous RF magnetic field is distinct from the SW spectrum excited by an RF current flowing through the nano-pillar. In section III, we perform unambiguous assignment of the resonance peaks to the different layers by experimental means. We determine which layer contributes mostly to the observed resonant signals by adding a direct current through the nano-pillar, that produces opposite spin transfer torques on each magnetic layer. In section IV, we analyze the spectra by theoretical means using both a two-dimensional analytical formalism and a three-dimensional micromagnetic simulation package, SpinFlow 3D. By careful comparison of the measured spectra to the calculations, the nature of the SW dynamics in the system is identified and the selection rules for SW spectroscopy in perpendicularly magnetized spin-valve nanostructures are established. This result is completed in section V by a study of the influence of symmetry breaking on the selection rules. This is obtained experimentally by introducing a tilt angle of the applied magnetic field, and in simulations by changing the shape of the nano-pillar. In the conclusion, we emphasize the importance of this work for phase synchronization of STNOs. The paper is arranged in such

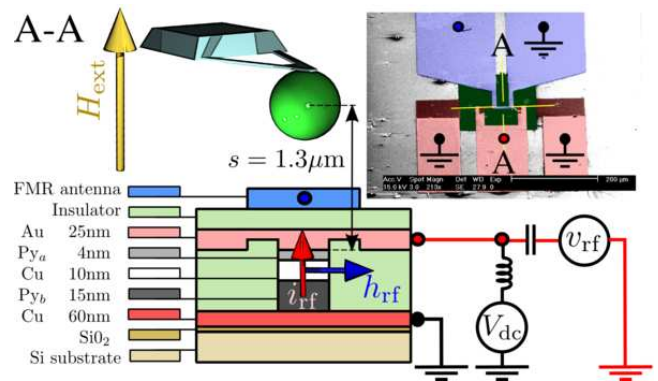


FIG. 1. (Color online) Schematic representation of the experimental setup used for this comparative spin-wave spectroscopic study. The magnetic sample is a circular nano-pillar comprising a thin Py_a and a thick Py_b magnetic layers separated by a Cu spacer. It is saturated by a large magnetic field \mathbf{H}_{ext} applied along its normal axis. A cantilever with a magnetic sphere attached at its tip monitors the magnetization dynamics inside the buried structure. The inset is a microscopy image (top view) of the two independent excitation circuits: in red the circuit allowing the injection of an RF current perpendicular-to-plane through the nano-pillar (i_{rf} , red arrow); in blue the circuit allowing the generation of an RF in-plane magnetic field (h_{rf} , blue arrow). The nano-pillar is at the center of the yellow cross-hair. The main figure is a section along the A – A direction.

a fashion so as to present the main results in the body of the text. A comprehensive appendix has been put at the end of the paper, where the details of the introduced material are developed.

II. FERROMAGNETIC RESONANCE FORCE SPECTROSCOPY

This section starts with a description of the nano-pillar sample, followed by a description of the MRFM instrument used for this spectroscopic study. Then, we compare the experimental SW spectra excited by an RF current flowing perpendicularly through the nano-pillar, as used in ST-FMR, and by a uniform RF magnetic field applied parallel to the layers, as used in standard FMR.

A. The lithographically patterned nanostructure

The spin-valve structure used in this study is a standard Permalloy ($\text{Ni}_{80}\text{Fe}_{20}=\text{Py}$) bi-layer structure sandwiching a 10 nm copper (Cu) spacer: the thicknesses of the thin Py_a and the thick Py_b layers are respectively $t_a = 4$ nm and $t_b = 15$ nm. Special care has been put in the design of the microwave circuit around the nano-pillar. The inset of FIG. 1 shows a scanning electron microscopy top view of this circuit. The nano-pillar is located at the center of the cross-hair, in the middle of

a highly symmetric pattern designed to minimize cross-talk effects between both RF circuits shown in blue and red, which provide two independent excitation means.

The nano-pillar is patterned by standard e-beam lithography and ion-milling techniques from the extended film, (Cu60 | Py_b15 | Cu10 | Py_a4 | Au25) with thicknesses expressed in nm, to a nano-pillar of nominal radius 100 nm. A precise control allows to stop the etching process exactly at the bottom Cu layer, which is subsequently used as the bottom contact electrode. A planarization process of a polymerized resist by reactive ion etching enables to uncover the top of the nano-pillar and to establish the top contact electrode. The top and bottom contact electrodes are shown in red tone in FIG. 1. These pads are impedance matched to allow for high frequency characterization by injecting an RF current i_{rf} through the device. The bottom Cu electrode is grounded and the top Au electrode is wire bounded to the central pin of a microwave cable. Hereafter, spectra associated to SW excitations by this part of the microwave circuit will be displayed in red tone. The nano-pillar is also connected through a bias-T to a dc current source and to a voltmeter through the same contact electrodes, which can be used for standard current perpendicular to the plane (CPP-GMR) transport measurements⁴⁴. In our circuit, a positive current corresponds to a flow of electrons from the Py_b thick layer to the Py_a thin layer and stabilizes the parallel configuration due to the spin transfer effect^{6,7}. The studies presented below will be limited to a dc current up to the threshold current for auto-oscillations in the thin layer.

The originality of our design is the addition of an independent top microwave antenna, whose purpose is to produce an in-plane RF magnetic field h_{rf} at the nano-pillar location. In FIG. 1 this part of the microwave circuit is shown in blue tone. The broadband strip-line antenna consists of a 300 nm thick Au layer evaporated on top of a polymer layer that provides electrical isolation from the rest of the structure. The width of the antenna constriction situated above the nano-pillar is 10 μm . Injecting a microwave current from a synthesizer inside the top antenna produces a homogeneous in-plane linearly polarized microwave magnetic field, oriented perpendicular to the stripe direction. Hereafter, spectra associated to SW excitations by this part of the microwave circuit will be displayed in blue tone.

B. Mechanical-FMR

The nano-fabricated sample is then mounted inside a Magnetic Resonance Force Microscope (MRFM), hereafter named mechanical-FMR³⁸. The whole apparatus is placed inside a vacuum chamber (10^{-6} mbar) operated at room temperature. The external magnetic field produced by an electromagnet is oriented out-of-plane, *i.e.*, along the nano-pillar axis \hat{z} . The mechanical-FMR setup allows for a precise control, within 0.2° , of the po-

lar angle between the applied field and \hat{z} . In our study, the strength of the applied magnetic field shall exceed the saturation field (≈ 8 kOe), so that the nano-pillar is studied in the saturated regime.

The mechanical detector is an ultra-soft cantilever, an Olympus Bio-Lever having a spring constant $k \approx 5$ mN/m, with a 800 nm diameter sphere of soft amorphous Fe (with 3% Si) glued to its apex. Standard piezo displacement techniques allow for positioning the magnetic spherical probe precisely above the center of the nano-pillar, so as to retain the axial symmetry. This is obtained when the dipolar interaction between the sample and the probe is maximal, by minimizing the cantilever resonance frequency, which is continuously monitored⁴¹.

The mechanical sensor is insensitive to the rapid oscillations of the transverse component in the sample, which occur at the Larmor precession frequency, *i.e.*, several orders of magnitude faster than its mechanical resonances. The dipolar force on the cantilever probe is thus proportional to the static component of the magnetization inside the sample. For our normally magnetized sample, this longitudinal component reduces to M_z . We emphasize that for a bi-layer system, the force signal integrates the contribution of both layers. Moreover, the local $M_z(\mathbf{r})$ in the two magnetic layers is weighted by the distance dependence of the dipolar coupling to the center of the sphere. In our case though, where the separation between the sphere and the sample is much larger than the sample dimensions, one can neglect this weighting and the measured quantity simplifies to the spatial average:

$$\langle M_z \rangle \equiv \frac{1}{V} \int_V M_z(\mathbf{r}) d^3\mathbf{r}, \quad (1)$$

where the chevron brackets stand for the spatial average over the volume of the magnetic body.

The mechanical-FMR spectroscopy presented below consists in recording by optical means the vibration amplitude of the cantilever either as a function of the out-of-plane magnetic field H_{ext} at a fixed microwave excitation frequency f_{fix} , or as a function of the excitation frequency f at a fixed magnetic field H_{fix} . This type of spectroscopy is called cw, for continuous wave, as it is monitoring the magnetization dynamics in the sample under a forced regime. A source modulation is applied on the cw excitation. It consists in a cyclic absorption sequence, where the microwave power is switched on and off at the cantilever resonance frequency, $f_c \approx 11.85$ kHz. The signal is thus proportional to $\langle \Delta M_z \rangle$, where Δ represents the difference from the thermal equilibrium state. The source modulation enhances the signal, recorded by a lock-in detection, by the quality factor $Q \approx 2000$ of the mechanical oscillator. The force sensitivity of our mechanical-FMR setup is better than 1 fN, corresponding to less than 10^3 Bohr magnetons in a bandwidth of one second³⁸. We note that this modulation technique does not affect the line shape in the linear regime, because the period of modulation $1/f_c$ is very large com-

pared to the relaxation times of the studied ferromagnetic system^{45,46}. Moreover, we emphasize that since the mechanical-FMR signal originates from the cyclic diminution of the spatially averaged magnetization inside the whole nano-pillar synchronous with the absorption of the microwave power, it detects all possible SW modes without discrimination^{39,40}.

Finally, we mention that the stray field produced by the magnetic sphere attached on the cantilever does affect the detected SW spectra. In our setup, the separation between the center of the spherical probe and the nano-pillar is set to $1.3 \mu\text{m}$ (see FIG. 1), which is a large distance considering the lateral size of the sample. At such distance, the coupling between the sample and the probe is weak³⁸ as it does not affect the profiles of the intrinsic SW modes in the sample. This is in contrast with the strong coupling regime, where the stray field of the magnetic probe can be used to localize SW modes below the MRFM tip⁴⁷. For our mechanical SW spectrometer, the perturbation of the magnetic sphere reduces to a uniform translation of all the peak positions⁴⁸ by -190 Oe (see section III B). In the following, all the SW spectra are recorded with the magnetic sphere at the same exact position above the nano-pillar.

C. RF magnetic field vs. RF current excitations

The comparative spectroscopic study performed by mechanical-FMR at $f_{\text{fix}} = 8.1 \text{ GHz}$ on the normally magnetized spin-valve nano-pillar is presented in FIG. 2. In these experiments, there is no dc current flowing through the device, and the spectra are obtained in the small excitation regime (precession angles less than 5° , see appendix B 1). The upper panel (a) shows the SW spectrum excited by a uniform RF magnetic field applied in the plane of the layers, while the lower panel (b) displays the SW spectrum excited by an RF current flowing perpendicularly through the magnetic layers. The striking result is that these two spectra are different: none of the SW modes excited by the homogeneous RF field is present in the spectrum excited by the RF current flowing through the nano-pillar, and vice versa.

Let us first focus on FIG. 2a, where the obtained absorption spectrum corresponds to the so-called standard FMR spectrum. Here, the output power of the microwave synthesizer at 8.1 GHz is set to $+3 \text{ dBm}$, which corresponds to an amplitude of the uniform linearly polarized RF magnetic field $h_{\text{rf}} \approx 2.1 \text{ Oe}$ produced by the antenna (see appendix B 1). In this standard FMR spectrum, only SW modes with non-vanishing spatial average can couple to the homogeneous RF field excitation. In field-sweep spectroscopy, the lowest energy mode occurs at the largest magnetic field. So, the highest field peak at $H_{\text{①}} = 10.69 \text{ kOe}$ should be ascribed to the uniform mode. Since this peak is also the largest of the spectrum, it corresponds to the precession of a large volume in the nano-pillar, *i.e.*, the thick layer must dominate in the

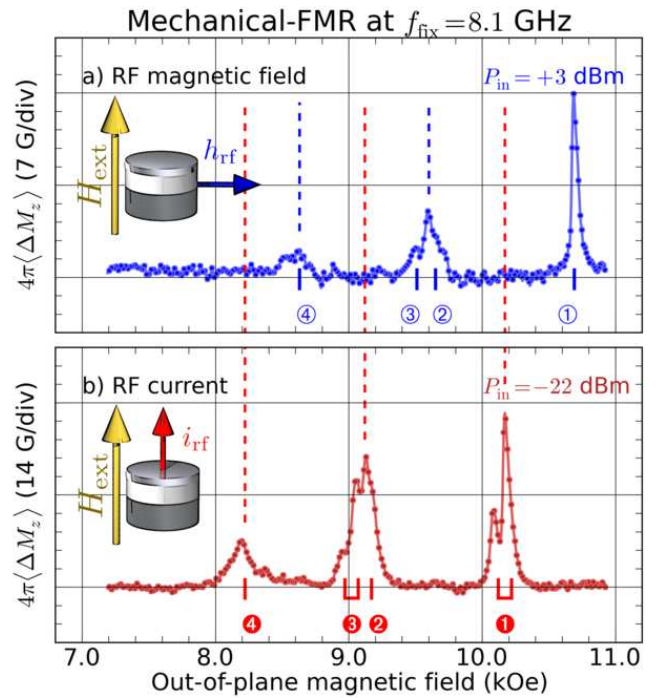


FIG. 2. (Color online) Comparative spectroscopic study performed by mechanical-FMR at $f_{\text{fix}} = 8.1 \text{ GHz}$, demonstrating that distinct SW spectra are excited by a uniform in-plane RF magnetic field (a) and by an RF current flowing perpendicularly through the layers (b). The positions of the peaks are reported in Table II.

dynamics. In mechanical-FMR, a quantitative measurement of the longitudinal magnetization is obtained^{39,49} (see appendix B 1). The amplitude of the peak at $H_{\text{①}}$ corresponds to $4\pi\langle\Delta M_z\rangle \approx 14 \text{ G}$, which represents a precession angle $\langle\theta\rangle \approx 3.1^\circ$. This sharp peak is followed by a broader peak with at least two maxima at $H_{\text{②}} = 9.65 \text{ kOe}$ and $H_{\text{③}} = 9.51 \text{ kOe}$, and at lower field, by a smaller resonance around $H_{\text{④}} = 8.64 \text{ kOe}$. Among these other peaks, there is the uniform mode dominated by the thin layer, which has to be identified and distinguished from higher radial index SW modes.

Let us now turn to FIG. 2b, corresponding to the spectroscopic response to an RF current of same frequency 8.1 GHz flowing perpendicularly through the nano-pillar. Here, the output power of the microwave synthesizer is -22 dBm , which corresponds to an rms amplitude of the RF current $i_{\text{rf}} \approx 170 \mu\text{A}$ (see appendix B 2). The SW spectrum is acquired under the *exact same conditions* as for standard FMR, *i.e.*, the spherical magnetic probe of the mechanical-FMR detection is kept at the same location above the sample. The striking result is that the position of the peaks in FIGS. 2a and 2b do not coincide. More precisely there seems to be a translational correspondence between the two spectra, which are shifted in field by about 0.5 kOe from each other. The lowest energy mode in the RF current spectrum occurs at $H_{\text{①}} = 10.22 \text{ kOe}$. This is again the most intense

peak, suggesting that the thick layer contributes to it, and $4\pi\langle\Delta M_z\rangle \simeq 26$ G, which represents a precession angle $\langle\theta\rangle \simeq 4.2^\circ$. This main resonance line is also split in two peaks, with a smaller resonance in the low field wing of the main peak, about 100 Oe away. At lower field, two distinct peaks appear at $H_{\ominus} = 9.17$ kOe and $H_{\otimes} = 9.07$ kOe and another peak is visible at $H_{\ominus} = 8.22$ kOe.

The fact that the two spectra of FIGS. 2a and 2b are distinct implies that they have a different origin. It will be shown in the theoretical section IV A 3 that the RF field and the RF current excitations probe two different azimuthal symmetries ℓ . Namely, only $\ell = 0$ modes are excited by the uniform RF magnetic field, whereas only $\ell = +1$ modes are excited by the orthoradial RF Oersted field associated to the RF current⁵⁰. The mutually exclusive nature of the responses to the uniform and orthoradial symmetry excitations is a property of the preserved axial symmetry, where the azimuthal index ℓ is a good quantum number, *i.e.*, different ℓ -index modes are not mixed and can be excited separately (see section IV A 2).

III. EXPERIMENTAL ANALYSIS

In this section, we first look at the effect of a continuous current flowing through the nano-pillar on the SW spectra in order to determine which layer contributes mostly to the resonant signals observed in FIG. 2. Due to the asymmetry of the spin transfer torque in each magnetic layer, the different SW modes are influenced differently depending on the layer in which the precession is the largest. Then, we briefly mention experiments, where spectroscopy is performed by monitoring the dc voltage produced by the magnetization precession in the hybrid nanostructure, and compared to mechanical-FMR. Finally, the analysis of the frequency-field dispersion relation and of the linewidth of the resonance peaks enables to extract the gyromagnetic ratio and the damping parameters in the thick and thin layers.

A. Direct bias current

To gain further insight about the peak indexation, we have measured the spectral evolution produced on the SW spectra of FIG. 2 when a finite dc current $I_{dc} \neq 0$ is injected in the nano-pillar. We recall that for our sign convention, a positive dc current stabilizes the thin layer and destabilizes the thick one due to the spin transfer torque, and vice versa^{6,7}. The results obtained by mechanical-FMR are reported in FIG. 3.

Let us first concentrate on FIG. 3a, in which the excitation that probes the different SW modes is the same as in FIG. 2a, *i.e.*, a uniform RF magnetic field. Two main features can be observed in the evolution of the SW spectra as I_{dc} is varied. First, the amplitude of the peak at H_{\ominus} smoothly increases with the positive current and smoothly decreases with the negative current. At

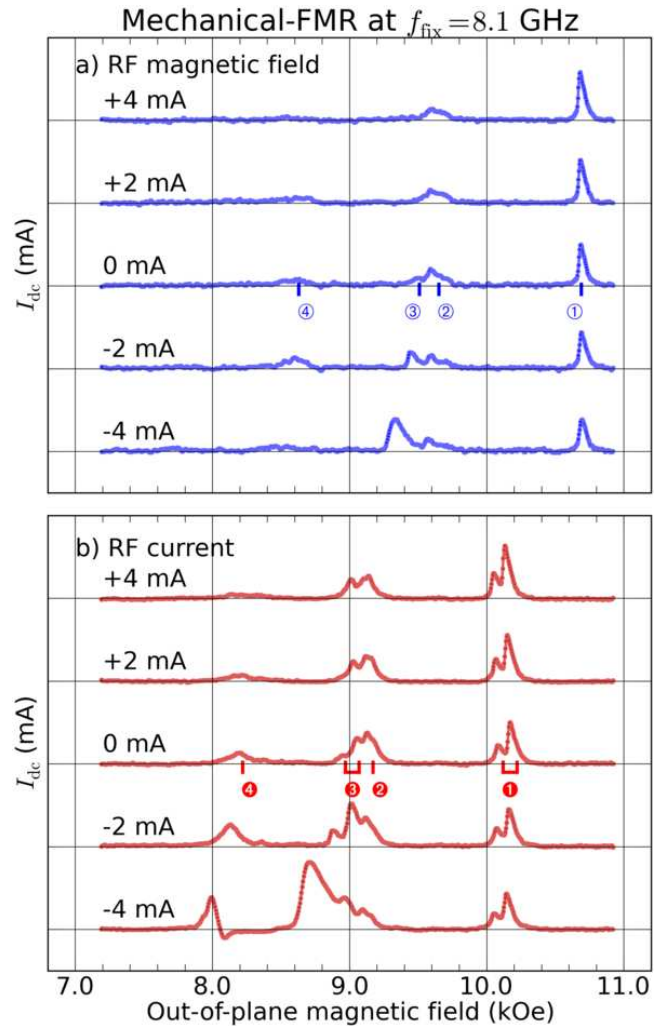


FIG. 3. (Color online) Evolution of the SW spectra measured at $f_{\text{fix}} = 8.1$ GHz by mechanical-FMR for different values of the continuous current I_{dc} flowing through the nano-pillar. The panel (a) corresponds to excitation by a uniform RF magnetic field and the panel (b) to excitation by an RF current through the sample.

the same time, the peak at H_{\otimes} , which is about five times smaller than the peak at H_{\ominus} when $I_{dc} = 0$ mA, almost disappears for positive current and strongly increases at negative current, until it becomes larger than the other peaks when $I_{dc} = -4$ mA. These two features are consistent with the effect of spin transfer if we ascribe the peak at H_{\ominus} to the uniform mode of mostly the thick layer and the peak at H_{\otimes} to the one of mostly the thin layer. More precisely, it is expected that in the sub-critical regime ($|I_{dc}| < I_{th}$, where I_{th} is the threshold current for auto-oscillations, $I_{th} < 0$ for the thin layer and $I_{th} > 0$ for the thick layer), the damping scales as $\alpha(1 - I_{dc}/I_{th})^{25,26}$ (see appendix A 1), where α is the Gilbert damping parameter. It means that the linewidth of a resonance peak that is favored by spin transfer should decrease as the current gets closer to I_{th} , and that its amplitude, which scales as

the inverse linewidth, should increase.

Although the effect on the peak amplitude noted above is clear in FIG. 3a, it is not on the linewidth. The reason is that in this experiment, the strength of the driving RF magnetic field is kept constant to $h_{\text{rf}} = 2.1$ Oe. As a result, the shape of the growing peaks in FIG. 3a becomes more asymmetric, which is a signature that the precession amplitude driven by the RF field is strong enough to change the internal field by an amount of the order of the linewidth. This leads to some foldover of the resonance line^{51,52}, a non-linear effect for which details are given in the appendix B 1. In other words, the distortion of the line shape as the peak amplitude increases prevents to see the diminution of its linewidth⁵³. It would be necessary to decrease the excitation amplitude as the threshold current is approached²⁶ so as to maintain the peak amplitude in the linear regime in order to reveal it.

The opposite signs of the spin transfer torques which influence the dynamics in the thin and thick layers are thus clearly seen in FIG. 3a. Their relative strengths can also be determined, as the amplitude of the peak at $H_{\text{③}}$ grows much faster with negative current than the one of the peak at $H_{\text{①}}$ with positive current. This is because the efficiency of the spin transfer torque is inversely proportional to the thickness of the layer^{6,7}. Whereas the precession angle in the thick layer does not vary much with I_{dc} (from $\approx 2.5^\circ$ at -4 mA to $\approx 3.5^\circ$ at $+4$ mA), the precession angle that can be deduced from $\langle \Delta M_z \rangle$ in the thin layer grows from almost zero at $I_{\text{dc}} = +4$ mA to more than 6° at $I_{\text{dc}} = -4$ mA. Moreover, the peak position $H_{\text{③}}$ shifts clearly towards lower field as the negative current is increased. This is due to the onset of spin transfer driven auto-oscillations in the thin layer, which occurs at a threshold current $I_{\text{th}} \lesssim -4$ mA and produces this non-linear shift¹⁹. We note, that such a value for the threshold current in the thin layer can be found from Slonczewski's model (see appendix A 1).

Let us now briefly discuss FIG. 3b, which shows the dependence on I_{dc} of the mechanical-FMR spectra excited by an RF current excitation. A similar dependence on I_{dc} of the resonance peaks in translational correspondence with FIG. 3a is observed. Again, a clear asymmetry is revealed depending on the polarity of I_{dc} and on the SW modes. The double peak at $H_{\text{①}}$ is favored by positive currents, hence it should be ascribed to mostly the thick layer precessing, while the double peak at $H_{\text{②}}$ is strongly favored by negative currents, hence it should be ascribed to mostly the thin layer precessing. Moreover, a careful inspection shows that the peak $H_{\text{②}}$, which looks single at $I_{\text{dc}} = 0$ mA, is actually at least double. We will explain this splitting of higher harmonics modes in section V B.

To summarize, the passage of a dc current through the nano-pillar enables to determine which layer mostly contributes to the observed SW modes, owing to the asymmetry of the spin transfer effect.

B. Voltage-FMR

Our experimental setup also allows to monitor the dc voltage produced across the nano-pillar by the precession of the magnetization in the bi-layer structure. A lock-in detection is used to measure the difference of voltage across the nano-pillar when the RF is on and off: $V_{\text{dc}} = V_{\text{on}} - V_{\text{off}}$. This can be done *simultaneously* to the acquisition of the mechanical-FMR signal, in the exact same conditions (see FIG. 1). Since the presentation of the experimental results requires a specific discussion, the details as well as the graphs will be published elsewhere. Here, we shall only reveal the three main features that can be noticed in the voltage-FMR spectra.

First, even at $I_{\text{dc}} = 0$, dc voltage peaks are produced across the nano-pillar at the same positions as the mechanical-FMR peaks observed in FIG. 2, with a difference of potential that lies in the 10 nV range for the precession angles excited here. It is ascribed to spin pumping and accumulation in the spin-valve hybrid structure^{54,55}. Second, these voltage resonance peaks are signed, namely, the SW modes favored at $I_{\text{dc}} < 0$ in FIG. 3a (for which the thin layer is dominating) produce a positive voltage peak, whereas those favored at $I_{\text{dc}} > 0$ (thick layer dominating) produce a negative voltage peak. This difference between the thick and thin layer contributions is ascribed to the asymmetry of the spin accumulation in the multi-layer stack⁵⁶. Third, the relative amplitudes of the voltage-FMR peaks are different from the mechanical-FMR ones. For instance, the voltage-FMR peak of the thin layer at $H_{\text{③}}$ is slightly *larger* than the peak at $H_{\text{①}}$ of the thick layer (and it has an opposite sign). This illustrates an important difference between the two detection schemes. While mechanical-FMR measures a quantity proportional to the precessing volume, $\langle \Delta M_z \rangle$, the voltage-FMR measures an interfacial effect. Therefore, when the same precession angle is excited in both layers, the voltage-FMR signal associated to each layer is approximately the same, whereas the mechanical-FMR signal from the thin layer is roughly four times smaller than the one from the thick layer, due to their relative thicknesses.

Finally, we mention that voltage-FMR spectroscopy can also record the intrinsic FMR spectrum of the nano-pillar, *i.e.*, in the absence of the spherical MRFM probe above it. This enables to check that the only effect introduced by the probe in mechanical-FMR is an overall shift of the SW modes spectra to lower field without any other distortion, and to quantify this shift, found to be -190 Oe⁵⁷.

C. Gyromagnetic ratio

A precise orientation of the applied magnetic field \mathbf{H}_{ext} along the normal \hat{z} of the sample (polar angle $\theta_H = (\hat{z}, \mathbf{H}_{\text{ext}}) = 0$) enables a direct determination of the modulus γ of the gyromagnetic ratio³⁸. By following

the frequency-field dispersion relation of the resonance peaks at H_{\ominus} and at H_{\otimes} (from 4.5 GHz to 8.1 GHz and from 6.2 GHz to 11 GHz, respectively) in our nano-pillar, it is found that $\gamma = 1.87 \times 10^7 \text{ rad.s}^{-1}.\text{G}^{-1}$ is identical in the thick and thin layers. Moreover, the value of γ measured in the nano-pillar is the same as in the extended reference film (see appendix B3 and Table I), confirming that the applied field is sufficient to saturate the two magnetic layers and is precisely oriented along \hat{z} .

The same result is obtained by following the evolution of the frequency-field dispersion relation presented in FIG. 4. Here, we take advantage of the broadband design of the electrodes which connect the nano-pillar to measure the FMR spectrum at fixed bias magnetic field, $H_{\text{fix}} = 10 \text{ kOe}$, by sweeping the frequency of the RF current through it. The data are plotted according to the frequency scale above FIG. 4a. At constant magnetic configuration (above the saturation field, *i.e.*, $\gtrsim 8 \text{ kOe}$), this frequency scale is in correspondence with field-sweep experiments performed at fixed RF frequency $f_{\text{fix}} = 8.1 \text{ GHz}$ through the affine transformation $H_{\text{ext}} - H_{\text{fix}} = 2\pi(f - f_{\text{fix}})/\gamma$, as seen from the field scale below FIG. 4b. This is a direct experimental check of the equivalence between frequency and field sweep experiments in the normally saturated state.

D. Damping parameters

From the FMR data presented above, we can also directly extract the damping parameters in each Permalloy layer. Indeed, in field-sweep spectroscopy in the normal orientation ($\theta_H = 0$), the full width at half-maximum (FWHM) ΔH of a resonance line is proportional to the excitation frequency $\omega/(2\pi)$ through the Gilbert constant α : $\Delta H = 2\alpha(\omega/\gamma)$ (see appendix A 1).

The linewidth of the peak at H_{\ominus} associated to mainly the thick layer in FIG. 2a is equal to $\Delta H_{\ominus} = 48 \text{ Oe}$, which corresponds to a damping $\alpha_{\ominus} = 0.88 \times 10^{-2}$. From the same mechanical-FMR spectrum, the linewidth of the peak at H_{\otimes} , associated to mainly the thin layer, cannot be easily extracted due to the proximity of the peak at H_{\oplus} . Owing to the interfacial origin of the voltage-FMR signal, the peak at H_{\otimes} is more distinguishable in the spectrum of the voltage-FMR (not shown), and its linewidth, $\Delta H_{\otimes} = 70 \text{ Oe}$, can be fitted. It corresponds to a damping $\alpha_{\otimes} = 1.29 \times 10^{-2}$.

The linewidths of the modes at H_{\bullet} and H_{\circ} can also be fitted and give similar results for the damping associated to each layer. In the case of the RF current excitation, a frequency-sweep spectrum can be acquired at a fixed bias magnetic field H_{fix} (see FIG. 4). In that case, the damping constant is simply obtained by $\alpha = \Delta f/(2f)$, where Δf is the width of the line centered at f . At $H_{\text{fix}} = 10 \text{ kOe}$, $f_{\bullet} = 7.37 \text{ GHz}$ and $\Delta f_{\bullet} = 0.12 \text{ GHz}$, which yield $\alpha_{\bullet} = 0.81 \times 10^{-2}$, and $f_{\circ} = 10.92 \text{ GHz}$ and $\Delta f_{\circ} = 0.33 \text{ GHz}$, which yield $\alpha_{\circ} = 1.5 \times 10^{-2}$.

In summary, we retain the following values for the

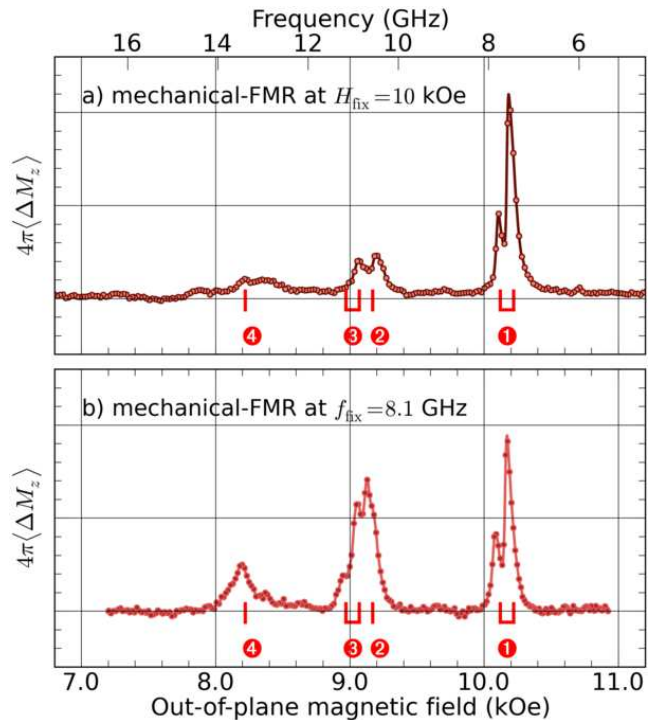


FIG. 4. (Color online) Frequency-field dispersion relation: the top spectrum (a) is measured at fixed bias field $H_{\text{fix}} = 10 \text{ kOe}$ by sweeping the frequency of the RF current i_{rf} through the nano-pillar. The bottom spectrum (b) is the same as in FIG. 2b, and is obtained by sweeping the magnetic field at fixed frequency $f_{\text{fix}} = 8.1 \text{ GHz}$ of i_{rf} . The top and bottom scales are in correspondence through the affine transformation $H_{\text{ext}} - H_{\text{fix}} = 2\pi(f - f_{\text{fix}})/\gamma$.

damping parameters in respectively the thin and the thick layers: $\alpha_a = (1.4 \pm 0.2) \times 10^{-2}$ and $\alpha_b = (0.85 \pm 0.1) \times 10^{-2}$. We have reported them, together with γ , in Table I.

These two values are in line with the ones obtained on the reference film, which have also been reported in Table I. Still, we observe that the linewidths in the nanostructure are systematically lower than the ones measured on the reference film. This is a constant characteristic that we associate to the confined geometry, which lifts most of the degeneracy (well separated SW modes) and thus strongly reduces the inhomogeneous part of the linewidth observed in the infinite layer^{15,26}. Rather, the inhomogeneities associated to the magnetic layers¹⁵ or to the confinement geometry will lead to some mode splitting in the nanostructure (see section VB). We have checked that the inhomogeneous contribution to the linewidth in the nano-pillar is weak, by following the dependence of the measured ΔH as a function of frequency. In fact, the increase of ΔH_{\otimes} from 70 Oe at 8.1 GHz to 105 Oe at 11 GHz is purely homogeneous.

Finally, the finding that the damping is larger in the thin layer than in the thick layer is ascribed to the adjacent metallic layers⁵⁸. In fact, non-local effects such

TABLE I. Magnetic parameters of the thin Py_a and thick Py_b layers measured by cavity-FMR on the reference film (top row) and by mechanical-FMR in the nano-pillar (bottom row).

$4\pi M_a$ (G)	α_a	$4\pi M_b$ (G)	α_b	γ ($\text{rad} \cdot \text{s}^{-1} \cdot \text{G}^{-1}$)
8.2×10^3	1.5×10^{-2}	9.6×10^3	0.9×10^{-2}	1.87×10^7
8.0×10^3	1.4×10^{-2}	9.6×10^3	0.85×10^{-2}	1.87×10^7

as the spin pumping effect^{54,59} and the spin diffusion in the adjacent normal layers by the conduction electrons yield an interfacial increase of the magnetic damping⁶⁰, stronger in the case of thin layers.

IV. THEORETICAL ANALYSIS

In this section, we first review a general formalism allowing the calculation of the discrete spectrum associated with SW propagation inside a confined body of arbitrary magnetic configuration. It is shown that in the two-dimensional (2D) axially symmetric case, different ℓ -index modes can be excited separately, as found experimentally in section II C. The classification of the SW modes in this case is also used to extract the parameters of each magnetic layer from the experimental FMR spectra. In a second part, we discuss the influence of the dynamic coupling between the magnetic disks, where the collective dynamics splits into binding and anti-binding modes. It is shown that in our experimental case, the dynamic dipolar coupling introduces a weak spectral shift, although its influence on the character of the SW modes is real. In the last part, a comparison to full three-dimensional (3D) micromagnetic simulations is performed in order to study in details the collective dynamics in the nano-pillar.

A. Analytical model

1. General theory

Below, we briefly review the general theory of linear SW excitations (see appendix A 1 for more details). We consider an arbitrary equilibrium magnetic configuration, where the local magnetization writes $M_s \hat{\mathbf{u}}$, with M_s the saturation magnetization and $\hat{\mathbf{u}}$ the unit vector along the local equilibrium direction (implicitly dependent on the spatial coordinates). The linearization of the *local* equation of motion is obtained by decomposing the instantaneous magnetization vector $\mathbf{M}(t)$ into a static and dynamic component⁶¹ (see FIG. 5). We shall use the fol-

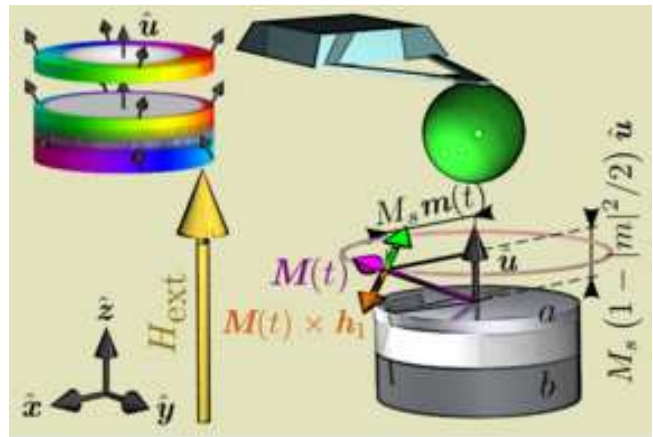


FIG. 5. (Color online) Schematic representation of the magnetization dynamics under continuous RF excitation. In the steady state, the torque exerted by the RF perturbation field \mathbf{h}_1 (orange arrow) compensates the torque exerted by the damping (green), and the local magnetization vector $\mathbf{M}(t)$ (purple) precesses at the Larmor frequency on a circular orbit around the local equilibrium direction (unit vector $\hat{\mathbf{u}}$). $\mathbf{M}(t)$ is the vector sum of a small oscillating component $M_s \mathbf{m}$ and a large static component $M_s (1 - |\mathbf{m}|^2/2)$, respectively transverse and parallel to $\hat{\mathbf{u}}$. The inset shows the simulated spatial distribution of $\hat{\mathbf{u}}$ inside the nano-pillar at $H_{\text{ext}} = 10$ kOe (see section IV C). In the white regions, the magnetization is aligned along the normal $\hat{\mathbf{z}}$ within 0.05° . In the colored regions, $\hat{\mathbf{u}}$ is flaring ($< 5^\circ$) in the radial direction (the hue indicates the direction of $\hat{\mathbf{u}} - \hat{\mathbf{z}}$ according to the color code defined in FIG. 6).

lowing ansatz:

$$\frac{\mathbf{M}(t)}{M_s} = \hat{\mathbf{u}} + \mathbf{m}(t) + \mathcal{O}(\mathbf{m}^2), \quad (2)$$

where the transverse component $\mathbf{m}(t)$ is the small dimensionless deviation ($|\mathbf{m}| \ll 1$) of the magnetization from the equilibrium direction. In ferromagnets, $|\mathbf{M}| = M_s$ is a constant of the motion, so that the local orthogonality condition $\hat{\mathbf{u}} \cdot \mathbf{m} = 0$ is required.

Substituting Eq. (2) in the lossless Landau-Lifshitz equation Eq. (A1) (see appendix A 1) and keeping only the terms linear in \mathbf{m} , one obtains the following dynamical equation for \mathbf{m} :

$$\frac{\partial \mathbf{m}}{\partial t} = \hat{\mathbf{u}} \times \hat{\Omega} * \mathbf{m}, \quad (3)$$

where here and henceforth, tensor operators are indicated by wide hat, the cross product is denoted by \times and the convolution product is denoted by $*$. The self-adjoint tensor operator $\hat{\Omega}$ represents the Larmor frequency:

$$\hat{\Omega} = \gamma H \hat{\mathbf{I}} + 4\pi\gamma M_s \hat{\mathbf{G}}, \quad (4)$$

where γ is the modulus of the gyromagnetic ratio, H is the scalar effective magnetic field, $\hat{\mathbf{I}}$ is the identity matrix, and $\hat{\mathbf{G}}$ is the linear tensor operator describing

the magnetic self-interactions. The later is the addition of several contributions $\widehat{\mathbf{G}}^{(d)} + \widehat{\mathbf{G}}^{(e)} + \dots$, respectively the magneto-dipolar interactions, the inhomogeneous exchange, etc... (see appendix A 2). The effective magnetic field \mathbf{H} is a vector aligned along $\hat{\mathbf{u}}$, whose norm is

$$H = \hat{\mathbf{u}} \cdot \mathbf{H}_0 - 4\pi M_s \hat{\mathbf{u}} \cdot \widehat{\mathbf{G}} * \hat{\mathbf{u}}, \quad (5)$$

the sum of the $\hat{\mathbf{u}}$ -component of \mathbf{H}_0 , the total applied magnetic field including the stray field of any nearby magnetic object (in our case, the adjacent magnetic layer in the nano-pillar and the spherical probe), reduced by the static self-interactions, which include the depolarization magnetic field along $\hat{\mathbf{u}}$ created by the static component of the magnetization.

SW modes \mathbf{m}_ν are by definition eigen-solutions of Eq. (3):

$$-i\omega_\nu \mathbf{m}_\nu = \hat{\mathbf{u}} \times \widehat{\mathbf{\Omega}} * \mathbf{m}_\nu. \quad (6)$$

Here ω_ν is the SW eigen-frequency and ν is a set of indices to enumerate the different modes.

The main properties of SW excitations follow from the eigen problem Eq. (6) and the fact that the operator $\widehat{\mathbf{\Omega}}$ is self-adjoint and real. One can show that the eigen solutions obey the closure relation

$$i \langle \overline{\mathbf{m}}_\nu \cdot (\hat{\mathbf{u}} \times \mathbf{m}_{\nu'}) \rangle = \mathcal{N}_\nu \delta_{\nu, \nu'}, \quad (7)$$

where δ is the Kronecker delta function and $\overline{\mathbf{m}}$ stands for the complex conjugate of \mathbf{m} . Here we have used the chevron bracket notation introduced in Eq. (1) to denote the spatial average. The quantities \mathcal{N}_ν are real normalization constants, which depend on the choice of eigen-functions \mathbf{m}_ν . If the equilibrium magnetization $\hat{\mathbf{u}}$ corresponds to a (local) minimum of the energy, then the operator $\widehat{\mathbf{\Omega}}$ is positive-definite. It follows that the ‘‘physical’’ modes with $\omega_\nu > 0$ have positive norm $\mathcal{N}_\nu > 0$. In this formalism, the eigen-frequencies ω_ν can be calculated as

$$\omega_\nu = \frac{\langle \overline{\mathbf{m}}_\nu \cdot \widehat{\mathbf{\Omega}} * \mathbf{m}_\nu \rangle}{\mathcal{N}_\nu}. \quad (8)$$

The importance of this relation is that the frequencies ω_ν calculated using Eq. (8) are variationally stable with respect to perturbations of the mode profile \mathbf{m}_ν . Thus, injecting some trial vectors inside Eq. (8) allows one to get approximate values of ω_ν with high accuracy⁶². The trial vectors should obey some simple properties: i) they should form a complete basis in the space of vector functions \mathbf{m} , ii) be locally orthogonal to $\hat{\mathbf{u}}$ and iii) satisfy appropriate boundary conditions at the edges of the magnetic body⁶³.

2. Normally magnetized disks

In this part, we shall establish a SW modes basis \mathbf{m}_ν for a normally magnetized disk. A specific feature of the

considered geometry is its azimuthal symmetry. Mathematically, this means that the operator $\hat{\mathbf{u}} \times \widehat{\mathbf{\Omega}}$ commutes with the operator $\widehat{\mathbf{R}}_z$ that describes an infinitesimal rotation about the $\hat{\mathbf{z}}$ axis, assuming that the boundary conditions are invariant under such a rotation.

This particular configuration allows us to classify the SW modes according to their behavior under the rotations in the (x, y) plane. Namely, SW eigen-modes are also eigen-functions of the operator $\widehat{\mathbf{R}}_z$ corresponding to a certain integer azimuthal number ℓ :

$$\frac{\partial \mathbf{m}}{\partial \phi} - \hat{\mathbf{z}} \times \mathbf{m} = -i(\ell - 1)\mathbf{m}. \quad (9)$$

Here, ϕ is the azimuthal angle of the polar coordinate system.

As one can see, Eq. (9) determines the vector structure of SW modes and their dependence on the angle ϕ . Namely, Eq. (9) for a fixed ℓ has two classes of solutions:

$$\mathbf{m}_\ell^{(1)} = \frac{1}{2}(\hat{\mathbf{x}} + i\hat{\mathbf{y}})e^{-i\ell\phi}\psi_\ell^{(1)}(\rho), \quad (10a)$$

and

$$\mathbf{m}_\ell^{(2)} = \frac{1}{2}(\hat{\mathbf{x}} - i\hat{\mathbf{y}})e^{-i(\ell-2)\phi}\psi_\ell^{(2)}(\rho), \quad (10b)$$

where the functions $\psi_\ell^{(1,2)}(\rho)$ describe the dependence of the SW mode on the radial coordinate ρ and have to be determined from the dynamical equations of motion. So, the azimuthal symmetry allows one to reduce the 2D (ρ and ϕ) vector equations to a one-dimensional (ρ) scalar problem.

Generally speaking, SW eigen-modes are certain linear combinations of both possible ℓ -forms Eqs. (10). The coupling of these two forms is due solely to the inhomogeneous dipolar interaction. In our experimental case (lowest energy modes of a relatively thin disk) one can completely neglect this coupling⁶⁴ and consider only the right-polarized form Eq. (10a). In the following we will drop the superscript (1) in $\mathbf{m}_\ell^{(1)}$ and $\psi_\ell^{(1)}$.

We shall now find an appropriate set of radial functions $\psi_\ell(\rho)$ to calculate the SW spectrum using Eq. (8). Here, we can take advantage of the variational stability of Eq. (8) and, instead of the exact radial profiles $\psi_\ell(\rho)$ (to find them one has to solve integro-differential equations), use some reasonable set of functions. Namely, it is known that the dipolar interaction in thin disks or prisms does not change qualitatively the profile of SW modes, but introduces effective pinning at the lateral boundaries⁶³. Therefore, we will use radial profiles of the form $\psi_\ell(\rho) = J_\ell(k_{\ell,n}\rho)$, where $J_\ell(x)$ is the Bessel function and $k_{\ell,n}$ are SW wave-numbers determined from the pinning conditions at the disk boundary $\rho = R$. For our experimental conditions ($t_a, t_b \ll R$), the pinning is almost complete, and we shall use $k_{\ell,n} = \kappa_{\ell,n}/R$, where $\kappa_{\ell,n}$ is the n -th root of the Bessel function of the ℓ -th order.

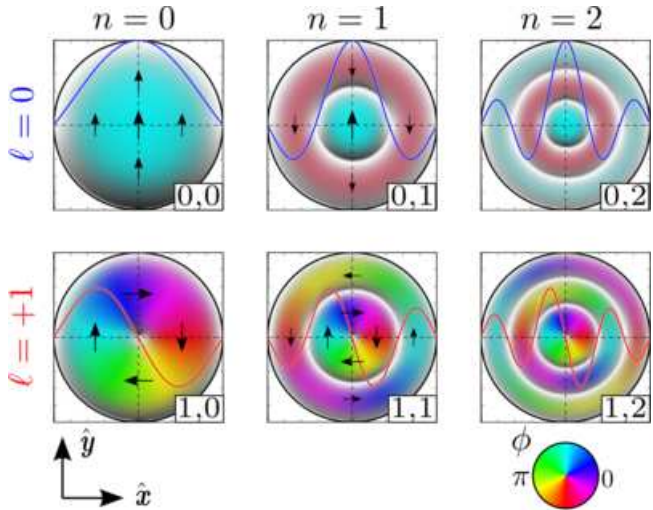


FIG. 6. (Color online) Color representation of the Bessel spatial patterns for different values of the azimuthal mode index ℓ (by row) and radial mode index n (by column). The arrows are a snapshot of the transverse magnetization \mathbf{m}_ν , labeled by the index $\nu = \ell, n$. All arrows are rotating synchronously in-plane at the SW eigen-frequency. In our coding scheme, the hue indicates the phase $\phi = \arg(\mathbf{m}_\nu)$ (or direction) of \mathbf{m}_ν , and the brightness the amplitude of $|\mathbf{m}_\nu|^2$. The nodal positions ($|\mathbf{m}_\nu| = 0$) are marked in white.

FIG. 6 shows a color representation of the Bessel spatial patterns for different values of the index $\nu = \ell, n$. We restrict the number of panels to two values of the azimuthal mode index, $\ell = 0, +1$, with the radial index varying between $n = 0, 1, 2$. In our color code, the hue indicates the phase (or direction) of the transverse component \mathbf{m}_ν , while the brightness indicates the amplitude of $|\mathbf{m}_\nu|^2$. The nodal positions are marked in white. A node is a location where the transverse component vanishes, *i.e.*, the magnetization vector is aligned along the equilibrium axis. This coding scheme provides a distinct visualization of the phase and amplitude of the precession profiles. The black arrows are a snapshot of the \mathbf{m}_ν vectors in the disk and are all rotating synchronously in-plane at the SW eigen-frequency.

The top left panel shows the $\nu = 0, 0$ ($\ell = 0, n = 0$) mode, also called the uniform mode. It usually corresponds to the lowest energy mode since all the vectors are pointing in the same direction at all time. Below is the $\ell = +1, n = 0$ mode. It corresponds to SWs that are rotating around the disk in the same direction as the Larmor precession. The corresponding phase is in quadrature between two orthogonal positions and this mode has a node at the center of the disk. The variation upon the $n = 0, 1, 2$ index (ℓ being fixed) shows higher order modes with an increasing number of nodal rings. Each ring separates regions of opposite phase along the radial direction. All these spatial patterns preserve the rotation invariance symmetry.

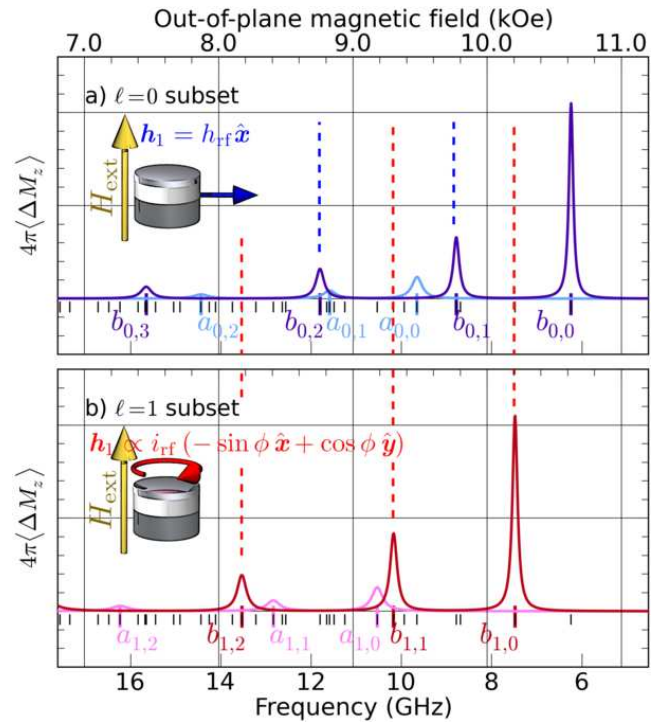


FIG. 7. (Color online) Analytically calculated spectra at $H_{\text{fix}} = 10$ kOe using the set of Bessel functions (see FIG. 6) as the trial eigen-vectors. The panel (a) shows the linear response to a uniform excitation field $\hat{\mathbf{h}}_1 = \hat{\mathbf{x}}$ and the panel (b) to an orthoradial excitation field $\hat{\mathbf{h}}_1 = -\sin \phi \hat{\mathbf{x}} + \cos \phi \hat{\mathbf{y}}$. A light (dark) color is used to indicate the energy stored Eq. (12) in the thin Py_a and thick Py_b layers.

3. Selection rules

Using the complete set of Bessel functions in Eq. (8), one can obtain analytically the discrete spectrum of eigen-values for both the thin and thick layers. The details of the numerical application can be found in appendix A 2. The spectral values are displayed in FIG. 7 using vertical ticks labeled $\nu = j\ell n$, where $j = a, b$ indicates the precessing layer, and ℓ, n the azimuthal and radial mode indices. They are calculated at fixed applied field $H_{\text{fix}} = 10$ kOe and placed on the graphs according to the frequency scale below FIG. 7b, which is in correspondence with the field scale above FIG. 7a (see III C for the equivalence between field- and frequency-sweep experiments).

The comparison with the experimental data in FIGS. 2a and 2b shows that the coupling to an external coherent source depends primarily on the ℓ -index. Indeed, this index carries the discriminating symmetry in SW spectroscopy⁶⁵. This is because the excitation efficiency is proportional to the overlap integral

$$h_\nu = \frac{\langle \overline{\mathbf{m}_\nu} \cdot \mathbf{h}_1 \rangle}{\mathcal{N}_\nu}, \quad (11)$$

where $\mathbf{h}_1(\mathbf{r})$ is the spatial profile of the external exci-

tation field. It can be easily shown that a uniform RF magnetic field, $\mathbf{h}_1 = h_{\text{rf}}\mathbf{x}$, can only excite $\ell = 0$ SW modes. We have shown in FIG. 7a the predicted position of these modes with blue tone ticks. Obviously the largest overlap is obtained with the so-called uniform mode ($n = 0$). Higher radial index modes ($n \neq 0$) still couple to the uniform excitation but with a strength that decreases as n increases^{37,66}. The $\ell \neq 0$ normal modes, however, are hidden because they have strictly no overlap with the excitation. The comparison with the experimental spectrum in FIG. 2a confirms that conventional FMR⁶⁷ probes only partially the possible SW eigen-modes, along the $\ell = 0$ -index value. In contrast, the RF current-created Oersted field, $\mathbf{h}_1 = h_{\text{Oe}}(\rho)(-\sin\phi\hat{\mathbf{x}} + \cos\phi\hat{\mathbf{y}})$ has an orthoradial symmetry and can only excite $\ell = +1$ SW modes. We have shown in FIG. 7b the predicted position of these modes with red tone ticks. They are in good agreement with the resonance positions observed in FIG. 2b. We also note that the $\ell = 0$ and $\ell = +1$ spectra calculated analytically bear similar a/b and n index series as a function of energy. This explains why the two spectra in FIGS. 2a and 2b look in translational correspondence with each other. We emphasize that the same translational correspondence would have been observed for any higher azimuthal order $\ell > 1$ index spectra.

From the coupling to the excitation field expressed by Eq. (11), one can also calculate the mechanical-FMR signal $\propto \langle \Delta M_z \rangle$, proportional to the energy stored in the magnetic system^{39,45}. For an arbitrary pulsation frequency ω ,

$$4\pi \langle \Delta \mathbf{M} \cdot \hat{\mathbf{u}} \rangle \simeq 4\pi M_s \sum_{\nu} \frac{\gamma^2 |h_{\nu}|^2}{(\omega - \omega_{\nu})^2 + \Gamma_{\nu}^2} \mathcal{N}_{\nu}, \quad (12)$$

where the SW damping rate Γ_{ν} is given by Eq. (A8) in appendix A 1. Eq. (12) is derived under the approximation that the only relevant coefficients in the damping matrix are the diagonal terms. It has been used to compute the relative peak amplitudes in the analytically calculated spectra of FIG. 7.

4. Comparison with experiments

The analytical model outlined in sections IV A 1 and IV A 2 can be used to analyze the experimental spectra of FIG. 2, and to extract some useful parameters of the nano-pillar. More details can be found in the appendix A 2 along with an approximate expression for the SW frequencies in the form of Kittel's traditional formula (with renormalized values of the effective self-demagnetization fields). This Kittel's formula, derived for the $\ell = 0$ spectrum, should be used to analyze the SW spectrum excited by a uniform RF field to yield the correct values of the magnetization in our nano-pillar. Identifying the experimental peaks at H_{Oe} and H_{O} as the lowest energy modes of the thin Py_a and thick Py_b layers yields their respective magnetizations $4\pi M_a = 8.0 \times 10^3$ G

and $4\pi M_b = 9.6 \times 10^3$ G, see Eq. (A32). These values have been reported in Table I, together with those measured in the reference film (see appendix B 3). The magnetizations extracted in the nano-pillar are the same as in the extended film. The only small difference concerns the magnetization of the thin layer, which is 200 G lower in the nanostructure than in the reference film (where $4\pi M_a = 8.2 \times 10^3$ G). We attribute this to some interdiffusion between Py and Cu or Au at the interfaces of the thin layer, which can happen during the etching process of the nano-pillar.

Second, the separation between SW modes crucially depends on the lateral confinement in the nano-pillar and thus on the precise value of its radius. Experimentally, the measured field separation between the two first peaks in FIG. 2a (FIG. 2b), which differ by an additional node in the radial direction, is $H_{\text{O}} - H_{\text{Oe}} = 1.04$ kOe ($H_{\text{O}} - H_{\text{Oe}} = 1.05$ kOe). Using the nominal radius 100 nm in the analytical model predicts that consecutive n -index mode ($n = 0$ and $n = 1$ modes) should be separated by 1.33 kOe, which is larger than the observed value. This separation drops to 1.05 kOe for a larger disk radius $R = 125$ nm, which we thus refer to as the radius of our nano-pillar. This value of R also allows to estimate the shift between the $\ell = 0$ and $\ell = +1$ spectra, found to be 530 Oe, in good agreement with the experimental value $H_{\text{O}} - H_{\text{Oe}} = 470$ Oe observed in FIG. 2.

B. Influence of dipolar coupling between different layers

In the treatment above we have neglected the dynamic coupling between the two magnetic disks in dipolar interaction. In general, the interaction between two identical magnetic layers will lead to the hybridization of the same ν -index mode of each layer into two collective modes: the acoustic mode, where the layers are precessing in phase, and the optical mode, where they are precessing in anti-phase. This has been observed in interlayer-exchange-coupled thin films⁶⁸ and in trilayered wires where the two magnetic stripes are dipolarly coupled⁶⁹. In the case where the two magnetic layers are not identical (different geometry or magnetic parameters), this general picture continues to subsist. Although both isolated layers have eigen-modes with different eigen-frequencies, the collective magnetization dynamics still splits in a binding and anti-binding state. But here, the precession of magnetization can be more intense in one of the two layers and the spectral shift of the coupled SW modes with respect to the isolated SW modes is reduced, as it was observed in both the dipolarly⁶⁹ and exchange-coupled cases⁷⁰.

Here, we assume that the dominant coupling mechanism between the Py layers is the magnetic dipolar interaction. We neglect any exchange coupling between the magnetic layers mediated through the normal spacer or any coupling associated to pure spin currents¹⁴ in our all-metallic spin-valve structure. To analyze the influence of

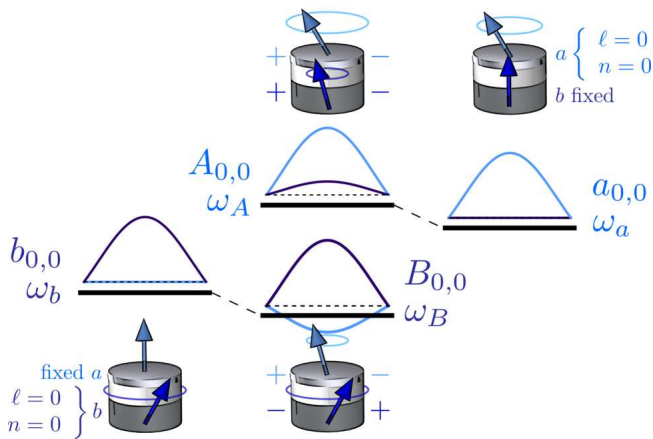


FIG. 8. (Color online) Schematic representation of the coupled dynamics between two different magnetic disks. Here, ω_b , the eigen-frequency of the lowest energy precession mode in the thick layer (the thin layer being fixed at equilibrium) is smaller than ω_a , the one in the thin layer (the thick layer being fixed at equilibrium). When the two disks are dynamically coupled through the dipolar interaction, the binding state B corresponds to the two layers oscillating in anti-phase at ω_B , with the precession occurring mostly in the thick layer, whereas the anti-binding state A corresponds to the layers oscillating in phase at ω_A , with the precession mostly in the thin layer. This is shown by displaying the dipolar charges and the precession profile $\mathbf{m}(\rho)$ in each layer using a light (dark) color to represent the contribution of the thin (thick) layer.

the dipolar coupling between the two magnetic layers, one can complement the perturbation theory derived in the previous section IV A and in the appendix A 1. Denoting c_j , the SW amplitudes in j -th disk, one can get from Eq. (A6):

$$\frac{dc_a}{dt} = -i\omega_a c_a + i\gamma h_{a,b} c_b, \quad (13a)$$

$$\frac{dc_b}{dt} = -i\omega_b c_b + i\gamma h_{b,a} c_a, \quad (13b)$$

where ω_j is the frequency of the j -th disk ($j = a, b$) with account of only the static field of the j' -th disk ($j' = b, a$) (*i.e.*, with $\mathbf{M}_{j'}$ fixed at equilibrium, see FIG. 8). The cross term $h_{j,j'}$ is given by

$$h_{j,j'} = -\frac{4\pi M_{j'}}{\mathcal{N}_j} \langle \overline{\mathbf{m}}_j \cdot \widehat{\mathbf{G}}^{(d)} * \mathbf{m}_{j'} \rangle_j. \quad (14)$$

Here, $\widehat{\mathbf{G}}^{(d)}$ represents the magneto-dipolar interaction, $M_{j'}$ is the saturation magnetization of the j' -th disk and the averaging goes over the volume of j -th disk. Thus, $h_{j,j'}$ is the average over the j -th mode of the magnetic field created by the magnetization of the j' -th disk. It can be shown that the overlap defined in Eq. (14) is maximum between mode pairs bearing similar wave-numbers in each layer (*i.e.*, the same set of indices ν)⁶⁹. This is the reason why dropping the index ν in Eqs. (13) and (14) is a reasonable approximation.

The anti-binding (A) and binding (B) eigen-frequencies of Eqs. (13) have the form

$$\omega_{A,B} = \frac{\omega_a + \omega_b}{2} \pm \sqrt{\left(\frac{\omega_a - \omega_b}{2}\right)^2 + \Omega^2}, \quad (15)$$

where

$$\Omega^2 = \gamma^2 h_{a,b} h_{b,a}. \quad (16)$$

In the case when the dipolar coupling is small ($\Omega \ll |\omega_a - \omega_b|$), the eigen-frequencies can be written as (we assume $\omega_a > \omega_b$)

$$\omega_A = \omega_a + \frac{\Omega^2}{\omega_a - \omega_b}, \quad (17)$$

$$\omega_B = \omega_b - \frac{\Omega^2}{\omega_a - \omega_b}. \quad (18)$$

These equations can be used for quantitative purposes when $\Omega/|\omega_a - \omega_b| < 0.3$ in which case they describe frequency shift with accuracy better than 10%. Thus, the larger of the frequencies (ω_a) shifts up by

$$\Delta\omega = \frac{\Omega^2}{\omega_a - \omega_b}, \quad (19)$$

while the smaller one (ω_b) shifts down by the same amount. This effect is summarized in FIG. 8.

A numerical estimate of the coupling strengths $h_{a,b}$ and $h_{b,a}$ between the lowest energy SW modes in each disk can be found in appendix A 2. The obtained result is very close to the approximate estimation used in Ref.⁷¹, where the spatial structure of the interacting SW modes is ignored to calculate the dipolar coupling between uniformly precessing disks. For the experimental parameters, $\Omega/2\pi \simeq 0.5$ GHz. This coupling is almost an order of magnitude smaller than the frequency splitting $\omega_a - \omega_b$, caused, mainly, by the difference of effective magnetizations of two disks: $\gamma 4\pi(M_b - M_a) \simeq 2\pi \cdot 4.5$ GHz. As a result, the shift of the resonance frequencies due to the dipolar coupling is negligible, $\Delta\omega/2\pi \simeq 0.06$ GHz.

Using Eqs. (13), one can also estimate the level of mode hybridization due to the dipolar coupling. For instance, at the frequency $\omega_A \approx \omega_a$, the ratio between the precession amplitudes in the two layers is given by

$$|c_b/c_a|_{\omega_A} = \Delta\omega/(\gamma h_{a,b}) \simeq \frac{\Omega}{\omega_a - \omega_b}. \quad (20)$$

For the experimental parameters, $\Omega/(\omega_a - \omega_b) \approx 0.1$, *i.e.*, the precession amplitude in the disk b is about 10 % of that in the disk a . Thus, although the dipolar coupling induces a small spectral shift (second order in the coupling parameter, Eq. (19)), its influence in the relative precession amplitude is significant (first order in the coupling parameter, Eq. (20)). Finally, we point that here the dipolar coupling is anti-ferromagnetic, and that the binding (lower energy) mode B always corresponds to the thick layer mainly precessing, with the thin layer vibrating in anti-phase, and vice-versa for the anti-binding (in-phase) mode A (see dipolar charges in FIG. 8).

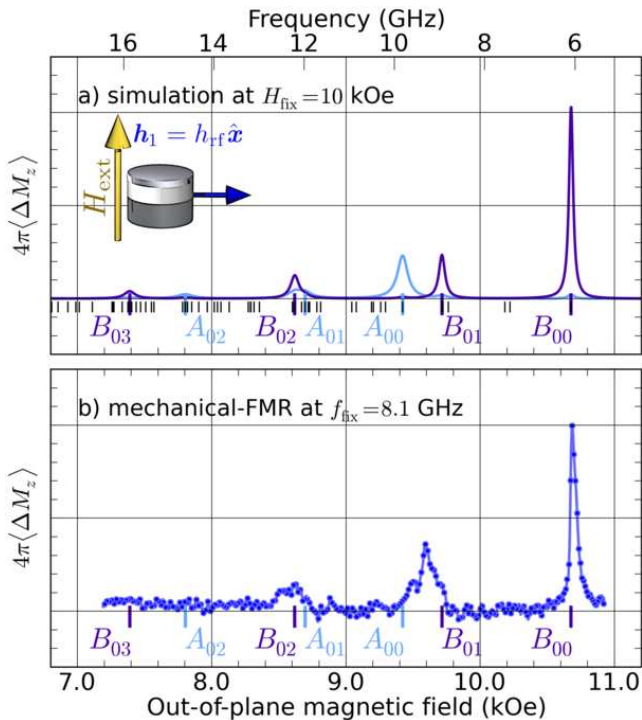


FIG. 9. (Color online) Panel (a) is the numerically calculated spectral response to a uniform excitation field $\mathbf{h}_1 \propto \hat{x}$, from a 3D micromagnetic simulation performed at $H_{\text{fix}} = 10$ kOe. The peaks are labeled according to their precession profiles shown in FIG. 11. A light (dark) color is used to indicate the energy stored in the thin (thick) layer. Panel (b) recalls the experimental spectrum measured by mechanical-FMR when exciting the nano-pillar by a homogeneous RF magnetic field at $f_{\text{fix}} = 8.1$ GHz.

C. Micromagnetic simulations

In the analytical formalism presented above, several approximations have been made. For instance, we have assumed total pinning at the disks boundary for the SW modes and no variation of the precession profile along the disks thicknesses (2D model), and we have neglected the dependence on ν of the dynamic dipolar coupling. Still, it allows to extract important parameters in our nano-pillar, such as its radius and the magnetization in both layers. It also describes the influence of the dynamic dipolar coupling on the position and collective character of the SW modes.

Instead of developing a more complex analytical formalism, we have performed innovative 3D micromagnetic simulations in order to go beyond the approximations mentioned above, and to unambiguously identify the SW modes observed in our nano-pillar sample. For that purpose, we have used a combination of micromagnetic simulation solvers available as part of SpinFlow 3D, a finite element based simulation platform for spintronics developed by In Silicio⁷². The steady state micromagnetic solver used to obtain numerical approximations of mi-

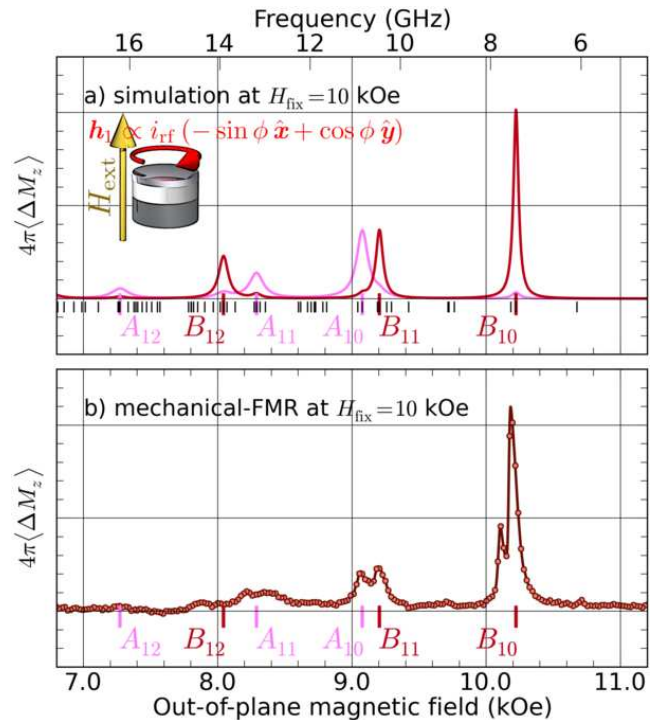


FIG. 10. (Color online) Panel (a) is the simulated spectral response to an orthoradial excitation field $\mathbf{h}_1 \propto -\sin\phi\hat{x} + \cos\phi\hat{y}$. Panel (b) recalls the experimental spectrum measured by mechanical-FMR for an RF current excitation.

cromagnetic equilibrium states is based on a weak formulation and Galerkin type finite element implementation of the very efficient projection scheme introduced in Ref.⁷³. A second numerical solver, a micromagnetic Eigen solver, has been used for fast calculations of lossless 3D SW eigen-modes. It is based on a finite element discretization of the generalized eigen-value problem defined by the linearized lossless magnetization dynamics in the vicinity of an arbitrary pre-computed equilibrium state, following an approach very similar to the one introduced in Ref.⁷⁴. The discrete generalized eigen-value problem is solved with an iterative Arnoldi method using the ARPACK library⁷⁵. In this calculation the full complexity of the 3D micromagnetic dynamics of the presently considered bilayer system is preserved. The solver outputs both the eigen-values by increasing energy order and the associated eigen-vectors. Several tens of SW eigen-modes can be accurately computed in a matter of few minutes of CPU time with a standard desktop PC, for magnetic thin film nano-structures with typical lateral sizes in the 100 nm range. This is two to three orders of magnitude faster compared to the required computation time when using more traditional approaches for micromagnetic computation of SW eigen-modes, which are typically based on the Fourier component analysis of time series generated by the solution of the full non-linear Landau-Lifshitz-Gilbert equation⁷⁶. Finally, a quite generic linear response solver, implement-

ing among other things the spectral decomposition of the MRFM signal as expressed in Eqs. (11), (12) and (A8), has been used to compute the MRFM spectra shown here.

To proceed, the nano-pillar is first discretized using unstructured meshing algorithms resulting in an average mesh size of 3.5 nm. This corresponds to a total number of vertices in the vicinity of 5×10^4 . The magnetization vector is interpolated linearly inside each cell (tetrahedra) – a valid approximation taking into account that the cell sizes are smaller than the exchange length $\Lambda_{\text{ex}} \simeq 5$ nm in Permalloy. The magnetic parameters introduced in the code are the ones reported in Table I, and the simulation incorporates the perturbing presence of the magnetic sphere attached on the cantilever. Moreover, the 10 nm thick Cu spacer is replaced by vacuum, so that the layers are only coupled through the dipolar interaction (spin diffusion effects are absent).

The next step is to calculate the equilibrium configuration in the nano-pillar at $H_{\text{ext}} = H_{\text{fix}} = 10$ kOe. The external magnetic field is applied exactly along \hat{z} and the spherical probe with a magnetic moment $m = 2 \times 10^{-10}$ emu is placed on the axial symmetry axis at a distance $s = 1.3$ μm above the upper surface of the nano-pillar. The convergence criterion introduced in the code is $|dM_z/M_j| < 2 \cdot 10^{-9}$ between iterations. The result shown in the inset of FIG. 5 reveals that the equilibrium configuration is almost uniformly saturated along \hat{z} . Still, a small tilt ($< 5^\circ$) of the magnetization, away from \hat{z} and along the radial direction, is observed at the periphery of the thick and thin layers.

The micromagnetic eigen solver is then used to compute the lowest eigen-values of the problem as well as the associated eigen-vectors. The discrete list of eigen-values under 18 GHz is shown as black vertical ticks at the bottom of FIGS. 9a and 10a. The precession patterns of the six eigen-vectors corresponding to the six lowest eigen-frequencies are shown in FIG. 11. The middle and right columns show the dynamics \mathbf{m} in the thin Py_a and thick Py_b layers, while the precession profiles along the median direction are shown on the left in light and dark colors, respectively. The resonance peaks are labeled according to the SW modes precession profiles and the eigen-values of the simulated peaks are reported in Table II.

From the eigen-vectors spatial patterns, one can compute their coupling (Eq. (11)) to a uniform RF field $\mathbf{h}_1 = h_{\text{rf}}\hat{x}$ and, with Eq. (12), the mechanical-FMR spectrum (FIG. 9a). The same procedure is repeated for the RF current-induced Oersted field $\mathbf{h}_1 \propto i_{\text{rf}}(-\sin\phi\hat{x} + \cos\phi\hat{y})$ excitation (FIG. 10a). Since the code gives access to the contribution of each layer, a light (dark) tone is used to indicate the vibration amplitude in the thin (thick) layer in the two figures. For comparison, the mechanical-FMR spectra of FIGS. 2a and 4a have been reported in FIGS. 9b and 10b, respectively. We have applied the same conversion between the frequency (top) and field (bottom) scales as discussed in section III C.

In FIG. 9a, the largest peak in the simulation occurs at

TABLE II. Comparative table of the resonance values for the SW modes, arranged in order of increasing energy. On the left are the consecutive peak locations measured experimentally. Experiments are performed at $f_{\text{fix}} = 8.1$ GHz (FIG. 2) or $H_{\text{fix}} = 10$ kOe (FIG. 4a). On the right are the simulated eigen-frequencies f at $H_{\text{fix}} = 10$ kOe. The conversion to field value H_{ext} is obtained through $H_{\text{ext}} - H_{\text{fix}} = 2\pi(f - f_{\text{fix}})/\gamma$.

Exp.	f (GHz)	H_{ext} (kOe)	Simu.	f (GHz)	H_{ext} (kOe)
①		10.69	B_{00}	6.08	10.68
①	7.37	10.22	B_{10}	7.44	10.22
②		9.65	B_{01}	8.95	9.71
③		9.51	A_{00}	9.82	9.42
②	10.48	9.17	B_{11}	10.47	9.20
③	10.92	9.07	A_{10}	10.85	9.08
④		8.64	A_{01}	11.98	8.69
④	13.41	8.22	A_{11}	13.19	8.29

the same field as the experimental peak at $H_{\text{①}}$. This lowest energy mode corresponds to the most uniform mode with the largest wave-vector and no node along the radial direction, thus it has the index $n = 0$. It has uniform phase along the azimuthal direction, which is the character of the $\ell = 0$ index. For this mode, the thick layer is mainly precessing, with the thin layer oscillating in anti-phase (binding index B), as can be seen from its spatial profile in FIG. 11. The same analysis can be made for the second peak, labeled B_{01} , which occurs close to the peak at $H_{\text{②}}$. It also corresponds to a resonance mainly of the thick layer, and its color representation shows that this is the first radial harmonic ($n = 1$), with one line of nodes in the radial direction. Again, the thin layer is oscillating in anti-phase, with the same radial index $n = 1$, as clearly shown by the mode profile along the median direction. The third peak is labeled A_{00} and is located close to the experimental peak at $H_{\text{③}}$. It corresponds this time to a uniform ($n = 0$) precession mainly located in the thin layer, in agreement with the experimental analysis presented in section III A. In this mode, the thick layer is also vibrating in phase with the thin layer (anti-binding index A).

We can also look at the relative amplitudes of precession in the two disks to quantify the dynamic coupling between the disks. From the profiles shown in FIG. 11, one can infer that for the fundamental mode B_{00} , the amplitude of precession is distributed with a ratio of about 3:1 between the thick (75%) and the thin layer (25%). For the mode A_{00} , the ratio is 8:1 in favor of the thin layer, which contributes to 89% of the precession amplitude (11% for the thick layer). These relative precession amplitudes were expected from the relative weight of the thick and thin layers and from the approximate analytical model presented in section IV B. The simulated field separation between the two coupled uniform modes $(\omega_{B_{00}} - \omega_{A_{00}})/\gamma = 1.28$ kOe compares also well with the 1.30 kOe estimate from the 2D model, with the dynamic dipolar coupling taken into account. Finally, one can check from the simulations the independence of

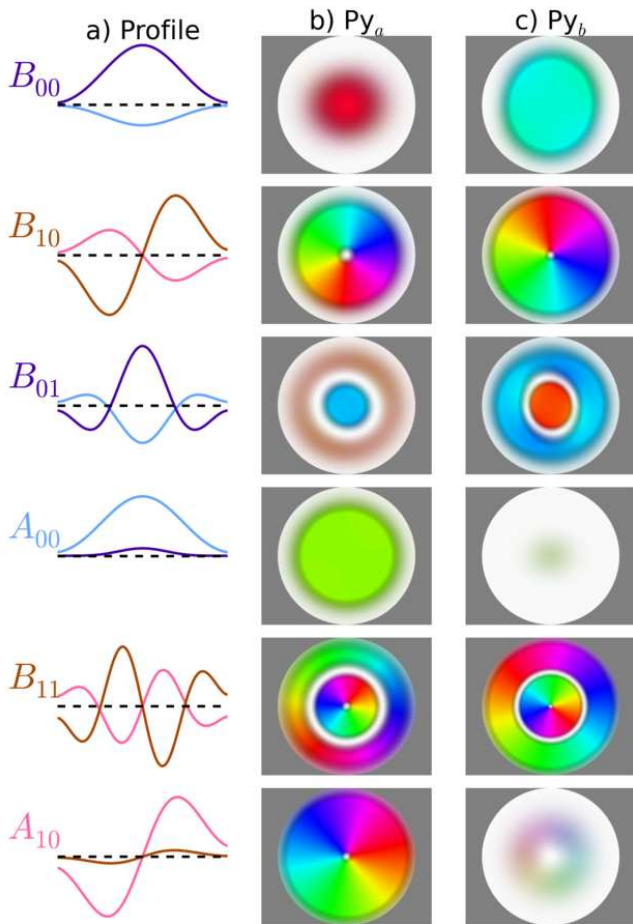


FIG. 11. (Color online) Simulated precession patterns of the eigen-vectors. Column (a) shows the precession profiles across the thin (light color) and thick (dark color) layers. Columns (b) and (c) show the dynamics in the thin Py_a and thick Py_b layers, respectively, with the color code defined in FIG. 6.

the precession profiles on the thickness. This confirms the validity of the 2D approximation and explains the performances of the analytical model.

We now briefly comment on the simulated spectrum of FIG. 10, which enables to identify the SW modes excited by the orthoradial Oersted field produced by the RF current flowing through the nano-pillar. From FIGS. 10 and 11, it is clear that the modes which couple to this excitation symmetry have a rotating phase in the azimuthal direction, characteristic of the $\ell = +1$ modes⁷⁷. We find that the SW modes of FIG. 10 show the same series of A/B and n indices as those in FIG. 9 (but their ℓ -index is different). This sustains the translational correspondence between the SW spectra of FIGS. 2a and 2b. Finally, we point out that, for all the modes displayed in FIG. 11, the pinning conditions at the boundaries of each disk are not trivial, which we attribute to the collective nature of the motion driven by the dipolar coupling⁷⁸. The general trend observed here is that the thin layer is less pinned than the thick layer for in-phase modes, and vice versa.

To summarize, the 3D micromagnetic simulations enable the identification (with three indices, A/B , ℓ and n) of the SW modes probed experimentally by both a uniform RF magnetic field and an RF current flowing through the nano-pillar, *i.e.*, of their respective selection rules. They confirm the experimental analysis performed in section III and give a deeper insight on the collective nature of the magnetization dynamics in the nano-pillar discussed in section IV B.

V. SYMMETRY BREAKING

In the following, we review some characteristic spectral features associated with the breaking of the axial symmetry in our experiment. First, we experimentally report on the appearance of $\ell = 0$ modes in the SW spectrum excited by an RF current flowing through the nano-pillar, when a small tilt angle is introduced between the applied field and the normal of the layers. This bridges the gap between our mechanical-FMR experiments and usual ST-FMR measurements^{25,26}. Second, we have simulated the spectral distortions introduced by breaking the cylindrical symmetry of the SW confinement potential. This enables to explain the lift of degeneracy in the SW spectrum, which leads to the splitting of modes.

A. Polar angle dependence

The dependence on the polar angle $\theta_H = (\hat{z}, \mathbf{H}_{\text{ext}})$ of the mechanical-FMR spectra excited by a uniform RF magnetic field and by an RF current flowing through the nano-pillar is presented in FIG. 12. Let us first focus on the conventional FMR spectra shown in FIG. 12a, acquired at three different polar angles from the exact perpendicularity, increasing by steps of 1° . The main effect here is the shift of the $\ell = 0$ SW modes spectrum towards lower field as θ_H increases, which has been explained in details in Ref.³⁸ for a single magnetic disk. It is due to the decrease of the demagnetizing field produced by the tilt of the equilibrium magnetization away from the normal. In fact, in each magnetic layer $j = a, b$, the uniform magnetization creates a non-uniform dipolar field $4\pi M_j \hat{\mathbf{G}}^{(d_j)} * \hat{\mathbf{u}}_j$, which is maximum in the exact normal configuration. The equilibrium direction $\hat{\mathbf{u}}_j$ is in the plane $(\hat{z}, \mathbf{H}_{\text{ext}})$ and makes a polar angle $\theta_j > \theta_H$ with the normal determined by Eq. (A34). It can be estimated that when $H_{\text{ext}} \approx 10$ kOe and θ_H increases from 0° to 2° , the equilibrium angles θ_a and θ_b of the static magnetization in the thin and thick layers linearly increases from 0° to $\approx 9^\circ$ and from 0° to $\approx 13^\circ$, respectively. This leads to a shift to lower field of the FMR spectrum by about 420 Oe (see appendix A 2), in agreement with the data. We also emphasize that, in fact, the profiles of the SW eigen-modes are affected by the breaking of axial symmetry, and that the pure $\ell = 0$ eigen-modes when $\theta_H = 0$ become mixed with $\ell \neq 0$ modes³⁸ when $\theta_H \neq 0$.

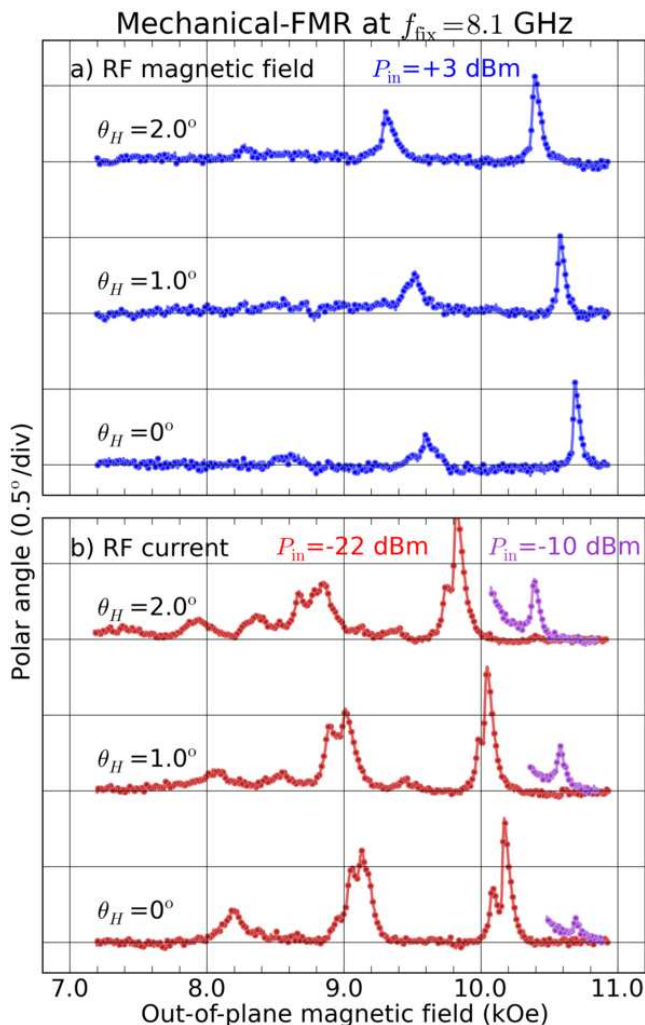


FIG. 12. (Color online) Dependence of the mechanical-FMR spectra excited by a uniform RF magnetic field (a) and by an RF current flowing through the nano-pillar (b) on the polar angle θ_H between the applied field and the normal to the layers. Superposed (in purple) is the behavior of the high field tail at larger power.

We now turn to the influence of the polar angle θ_H on the FMR spectra excited by an RF current ($i_{\text{rf}} = 170 \mu\text{A}$). The same global shift towards lower field as discussed above is observed in FIG. 12b by looking at the red spectra acquired with an increasing θ_H . But there is an important additional effect here. Whereas only $\ell = +1$ SW modes are excited by the RF current flowing through the nano-pillar in the exact perpendicular geometry, resonance peaks can also be detected at the positions of $\ell = 0$ SW modes when $\theta_H \neq 0$. Although the amplitudes of the $\ell = 0$ modes are not large in FIG. 12b, it is quite clear that they all grow as θ_H increases. In order to reveal this effect better, we have reported in purple on the same figure the resonance peak of the mode B_{00} excited with a +12 dB larger power ($i_{\text{rf}} \approx 680 \mu\text{A}$), as a function of θ_H .

Despite the large RF current excitation, its amplitude almost vanishes at $\theta_H = 0$. Then, it increases linearly with θ_H , until it becomes almost as large as when it is excited by the uniform RF field $h_{\text{rf}} \approx 2.1$ Oe used in FIG. 12a.

The experimental data and their analysis presented in the previous sections II to IV demonstrate that in the exact perpendicular configuration, only $\ell = +1$ modes are excited by the RF current flowing through the nano-pillar, due to the orthoradial symmetry of the induced RF Oersted field, Eq. (A14). Because there is no overlap between this particular excitation symmetry and the uniform azimuthal symmetry of the $\ell = 0$ modes, the latter do not couple to the RF current excitation. The fact that these hidden modes in the exact perpendicular configuration can be excited by introducing a small misalignment angle between the applied field and the normal to the nano-pillar \hat{z} is a striking result. It means that the selection rules associated to the RF current excitation change if the applied field is tilted away from \hat{z} , what we shall now explain.

Due to the smaller demagnetizing field in the thin magnetic disk than in the thick one (due to $M_a < M_b$), the equilibrium angle of the thin layer is smaller than in the thick layer, $\theta_a < \theta_b$, as obtained from Eq. (A34). For the parameters of our nano-pillar, $\beta = \theta_b - \theta_a \approx 2\theta_H$, at $H_{\text{ext}} \approx 10$ kOe and for a small angle θ_H . It means that if $\theta_H \neq 0$, the magnetization vectors in both layers are misaligned from each other by an angle $\beta = (\mathbf{M}_a, \mathbf{M}_b)$, so that the cross product $\hat{\mathbf{u}}_a \times \hat{\mathbf{u}}_b$ is finite and lies in the plane parallel to the layers, say along $\hat{\mathbf{x}}$. Thus, the spin transfer excitation $(2\pi\lambda)^{-1} i_{\text{rf}} \sin \beta \hat{\mathbf{x}}$ associated to the RF current flowing through the spin-valve nano-pillar^{25,26}, which is vanishing in the exact perpendicular configuration where $\beta = 0$, becomes finite if there is a small misalignment angle $\theta_H \neq 0$ (see Eqs. (A15) and (A16) in appendix A 1, $(2\pi\lambda)^{-1}$ is the spin transfer efficiency). Because this so-called ST-FMR excitation has the same symmetry as an in-plane uniform RF magnetic field, it is expected to excite SW modes having the $\ell = 0$ -index symmetry. Still, this excitation has to compete with the RF Oersted field excitation, which is independent of θ_H and is much larger in our configuration due to the small value of β ($< 5^\circ$). Therefore the amplitudes of the $\ell = +1$ modes are much larger than those of the $\ell = 0$ modes in FIG. 12b.

It is also clear that the amplitude of the mode B_{00} excited by the RF current (purple peaks in FIG. 12b) grows linearly with θ_H , as expected from the above discussion. We emphasize that a quantitative understanding of the amplitude of the peaks excited by ST-FMR would require to consider the collective nature of the dynamics in the nano-pillar and the asymmetry of spin transfer in the thick and thin magnetic layers. Finally, we note that the small signal observed at $\theta_H = 0$ should in principle vanish with the ST-FMR excitation. This reminiscent signal can be ascribed to a small misalignment of the applied field with respect to the normal to the nano-pillar (the precision on the orientation is 0.2°) or to a slight asymmetry of the RF current lines through the nano-

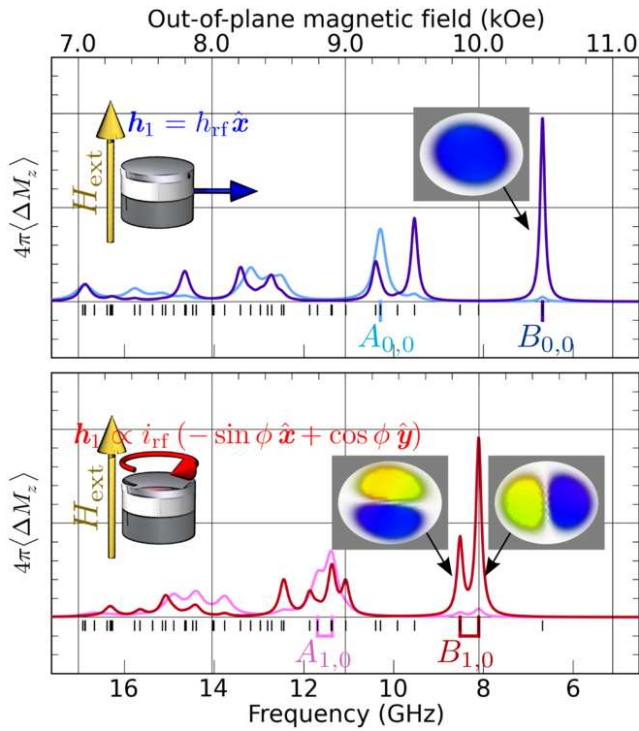


FIG. 13. (Color online) Simulated SW spectra for a nano-pillar with an elliptical section (see text). Linear response to a homogeneous RF magnetic field excitation (a) and to an orthoradial RF Oersted field excitation (b). The precession patterns of the lowest energy modes are shown in the insets.

pillar, which would induce a small asymmetry of the RF Oersted field, thereof adding a small in-plane uniform component to the orthoradial magnetic field.

To summarize, this study enables to derive the selection rules of the RF current excitation. In the exact perpendicular configuration, the magnetizations of both layers are aligned, and only $\ell = +1$ modes can be excited due to the orthoradial symmetry of the current-created Oersted field ($\ell = 0$ modes are hidden). But when a finite angle is introduced between the magnetizations in each layer by slightly tilting the applied field away from the normal, $\ell = 0$ modes can be excited by ST-FMR, which has the same symmetry as a uniform RF field excitation polarized in-plane.

B. Confinement asymmetries

As seen in section IV C, the 3D micromagnetic simulations enable to identify the SW modes observed in the experimental spectra. Still, the latter are more rich than the simulated power spectra, due to the splitting of some resonance peaks, which was noted in sections II C and III A. In particular, the experimental peak at H_{\bullet} , identified as the mode B_{10} , is clearly split in two, with a smaller resonance about 100 Oe away in the low field wing of the main peak, which is not the case in the sim-

ulation (see FIG. 10). The peaks at H_{\bullet} (identified as B_{11}) and at H_{\circ} (A_{10}) are also split, contrary to the simulations, where all these peaks are single. In contrast to these observations, the peak at H_{\circ} , which is the uniform mode B_{00} , is single both in the experimental and simulated spectra.

So, it seems that experimentally, the occurrence of the mode splitting depends on the mode index, whereas in 3D simulations, in which the nano-pillar has a perfect cylindrical shape, none of the resonance peaks is split. This suggests that the observed splittings are related to asymmetries in the confinement of the disks, and that the various SW modes are affected differently because they probe different regions. The fact that the double peak at H_{\bullet} depends on the tilt angle (see FIG. 12b) and is more or less pronounced depending on the direction in which the applied field is tilted from the normal (not shown) is another strong indication that some symmetry breaking in the lateral confinement is at the origin of this effect⁷⁹.

To support this idea, we have carried out new 3D micromagnetic simulations with the SpinFlow 3D package on a structure that break the perfect cylindrical symmetry of the nano-pillar. We have kept a perfectly flat structure, but we have used an elliptical cross-section. The long axis of the ellipse is 250 nm, while the short axis is 200 nm. The influence of this breaking of symmetry on respectively the $\ell = 0$ spectrum (RF field excitation) and the $\ell = +1$ spectrum (RF current excitation) is presented in FIG. 13.

Concentrating first on the standard FMR SW spectrum of FIG. 13a, one can see that the lowest energy mode B_{00} remains a single peak. This illustrates the intuitive idea that the uniform SW mode, where the oscillation power is mostly concentrated at the center, is rather not sensitive to change of the confinement at the periphery. The same behavior applies for the lowest energy mode of the thin layer, A_{00} .

The simulated SW spectrum of FIG. 13b shows a different sensitivity to the shape asymmetry. It is observed that the lowest energy mode with the $\ell = +1$ -index splits in two peaks, in contrast with the lowest energy $\ell = 0$ mode which remains a single peak. We also note that the satellite peak, induced by the elliptical confinement, is located in the low field wing of the main resonance, as in the experiments of FIG. 2b. The precession patterns shown in the two insets FIG. 13b reveal that the elliptical shape introduces some mixing between the $\ell = +1$ and $\ell = -1$ SW modes (the $\ell = -1$ mode corresponds to SWs that are rotating around the disk in the opposite direction as the Larmor precession). In a circular disk, these two modes are degenerate, and only the $\ell = +1$ mode couple to the orthoradial Oersted field excitation. But in the ellipse, the two eigen-modes split and become mixed, as shown by the two eigen-vectors displayed in FIG. 13b, which correspond to the linear combinations $J_1(\rho) + J_{-1}(\rho)$ and $J_1(\rho) - J_{-1}(\rho)$. The simulated spectrum of FIG. 13b reproduces well the main features of the mechanical-FMR spectrum of FIG. 2b, including the

splittings observed for the $\ell = +1$ SW modes (revealed even better by injecting a dc current through the nano-pillar, see FIG. 3b). Thus, a small elliptical shape produced during the nanostructuring of the nano-pillar is most likely responsible for the double peak observed at H_{\bullet} in FIG. 2b.

To summarize, the comparison between 3D simulations and experiments demonstrate that the observed mode splittings originates from a small asymmetry in the lateral confinement of the nano-pillar.

VI. CONCLUSION

In summary, we used the MRFM technique³⁸ to study the SW eigen-modes in the prototype of a STNO - a normally magnetized nano-pillar composed of two magnetic layers coupled by dipolar interaction.

In contrast to transport spectroscopy techniques^{22,25}, MRFM is sensitive to all SW modes excited in the sample³⁹ and is completely independent of the transport properties of the studied spin-valve sample. Therefore, MRFM provides an alternative and complementary view on the magnetization dynamics in hybrid magnetic nanostructures. The additional advantages of the MRFM technique are its high sensitivity (in this study, it was able to detect angles of precession as low as 1° in the thin magnetic layer) and its ability to operate on standard STNO devices buried under contact electrodes without a specific probe access to the studied sample⁴³.

Using MRFM, we were able to compare the SW spectra of a passive perpendicularly magnetized STNO-like sample excited by a uniform in-plane RF magnetic field and by an RF current flowing perpendicularly through the layers. We found that distinctly different SW modes (having azimuthal indices $\ell = 0$ and $\ell = +1$, respectively) are excited by the two above mentioned excitation methods. By studying the influence of a spin polarized dc current on the observed SW spectra we were able to determine which of the magnetic layers of the studied nanopillar plays the dominant role in the magnetization dynamics resulting in the appearance of each particular SW mode.

We also developed a simple analytic theory allowing to perform a comprehensive labeling of all the SW eigen-modes of a magnetic nanopillar in the studied axially symmetric case. This labeling requires three independent indices: the usual azimuthal and radial indices ℓ and n used for the SW modes of a single magnetic disk and an additional index referring to the binding or anti-binding (B or A) coupling between the two magnetic disks forming a nanopillar. The obtained experimental and analytic results were also compared to the results of 3D micromagnetic simulations obtained with the SpinFlow 3D package⁷², which confirmed the mode labeling obtained from the analytic theory.

Thus, we learned that in the axially symmetric case of a perpendicularly magnetized nano-pillar, the excita-

tions by the RF field the RF current lead to two mutually orthogonal (and mutually exclusive) sets of excited SW modes: only the $\ell = 0$ modes are excited by the uniform RF magnetic field, while only the $\ell = +1$ modes are excited by the RF current. Therefore, the ℓ -index, related to the azimuthal symmetry of the SW modes, is the discriminating parameter for the selection rules of the SW mode excitation.

Moreover, we have demonstrated experimentally and numerically that the mode selection rules are affected by the breaking of the axial symmetry of the studied nano-pillar, either by tilting the bias magnetic field or by making the sample cross-section elliptical. In particular, if the axial symmetry is broken by tilting the bias magnetic field, the $\ell = 0$ modes can also be excited by an RF current. This excitation is caused by the ST-FMR mechanism working when the magnetization vectors in the two magnetic layers of the nano-pillar are not collinear. Also, the importance of the dynamic dipolar interaction between the magnetic layers of the nano-pillar have been clearly demonstrated by our results.

We believe that our results are important for the optimization of the characteristics of nano-spintronic devices, and in particular STNOs, and for the experimental determination of the STNO parameters.

First of all, an accurate identification of the SW modes that can be excited in an STNO nano-pillar is necessary to understand the details of the high frequency STNO dynamics. The proposed identification of the nano-pillar SW modes can be used for the experimental determination of the nano-pillar characteristics, such as radius, static magnetization, gyromagnetic ratio, and dissipation. We note that in traditional STNO experiments, where the magnetization dynamics in a magnetic nano-pillar is excited by a spin-polarized bias current creating a significant Oersted magnetic field with the $\ell = +1$ symmetry, it is easy to mix-up the $\ell = 0$ and the $\ell = +1$ SW eigen-modes. The spectra of these modes are in almost translational correspondence, and the experimentally observed dependence of the mode frequencies on the bias magnetic field can be well described by the traditional Kittel expression (see *e.g.*¹¹). Thus, the possibly excited $\ell = +1$ mode can be easily interpreted as a $\ell = 0$ mode, which will lead to the apparent reduction of the “free” layer static magnetization necessary to fit the Kittel expression for the mode frequency. For instance, mislabeling the lowest energy mode of the $\ell = +1$ SW spectrum as the uniform mode ($\ell, n = 0, 0$) combined with a small misalignment of the applied field would lead to a discrepancy as large as 1 kG in our case.

Second, the fact that in most cases both magnetic layers of a nano-pillar take part in current-induced magnetization dynamics is very important for the correct identification of the excited SW modes. The collective (coupled) character of the SW modes in a nano-pillar can directly influence the magnitude of the spin transfer torque, which is dependent on the relative orientation of the magnetization vectors in the two magnetic lay-

ers. One might expect, that the efficiency of the spin transfer torque for a particular SW mode depends not only on which layer (“free” or “fixed”) is dominating the mode dynamics, but also on the coupling (in phase or anti-phase) between the magnetization precession in two layers. In our experimental case, the interlayer coupling is in-phase for the SW modes dominated by the dynamics in a “free” (thin) layer. To obtain an interlayer coupling which is anti-phase for the SW modes dominated by the dynamics of the thin layer would require for example to increase its magnetization compared to the “fixed” layer one.

Finally, it is important to note that the MRFM technique has allowed us to study spin transfer effects in the axially symmetric configuration of a perpendicularly magnetized nano-pillar, where the excitation of magnetization dynamics by ST-FMR vanishes due to the symmetry reasons. This geometry is rather important for applications as the excited SW modes have the maximum non-linear frequency shift coefficient¹⁹. This creates the maximum agility of the mode frequency with the bias current and, therefore, the maximum width of the synchronization band to the external periodic signal and to the large arrays of other STNOs¹⁹. Phase synchronization has been identified as a possible mean to dramatically increase the generated microwave power of these nano-oscillators and, at the same time, reduce their linewidth^{80–87}.

ACKNOWLEDGMENTS

This research was partially supported by the European Grant Master (NMP-FP7 212257) and by the French Grant Voice (ANR-09-NANO-006-01), by the contract from the U.S. Army TARDEC, RDECOM, and by the grants ECCS-1001815 and DMR-1015175 from the National Science Foundation of the USA.

Appendix A: Theoretical material

1. Equation of motion

In this appendix, we detail the derivation of the equations which govern the dynamics of a ferromagnetic layer in the presence of an external periodic excitation and of spin transfer, following the general formalism introduced in section IV A 1. For an isolated layer, the *local* dynamics (within the exchange length) of the magnetization vector is described by the Landau-Lifshitz (LL) equation:

$$\frac{1}{\gamma} \frac{\partial \mathbf{M}}{\partial t} = \mathbf{H} \times \mathbf{M} + \mathbf{h}(t) \times \mathbf{M}, \quad (\text{A1})$$

with γ being the modulus of the gyromagnetic ratio. The LL equation is written here in its perturbative form,

where the second term on the right-hand-side of Eq. (A1) represents the perturbation term. The field \mathbf{H} is the effective magnetic field:

$$\mathbf{H} = \mathbf{H}_0 - 4\pi \widehat{\mathbf{G}} * \mathbf{M}. \quad (\text{A2})$$

Here, \mathbf{H}_0 is the total static external magnetic field (possibly spatially-dependent) and the linear tensor self-adjoint operator $\widehat{\mathbf{G}}$ describes the magnetic self-interactions.

Considering only the linear processes, we can represent the time dependent (out-of-equilibrium) part of the magnetization as a series over the SW eigen-modes:

$$\begin{aligned} \mathbf{M}(t, \mathbf{r}) - M_s \hat{\mathbf{u}}(\mathbf{r}) &\approx \mathbf{m}(t, \mathbf{r}) \\ &\approx \sum_{\nu} c_{\nu}(t) \mathbf{m}_{\nu}(\mathbf{r}) + \text{c.c.}, \end{aligned} \quad (\text{A3})$$

where M_s is the saturation magnetization of the layer. Here, c.c. stands for the complex-conjugated part. The coefficients $c_{\nu}(t)$ are time-dependent SW amplitudes.

The second term on the left-hand-side of Eq. (A1) represents the perturbations from the equilibrium state, including the non-adiabatic contributions. The non-conservative perturbation magnetic field $\mathbf{h}(t)$ may depend on time and be a function of the magnetization distribution $\mathbf{M}(t)$. It can be approximately represented as:

$$\mathbf{h}(t) = \mathbf{h}_1(t) + \widehat{\mathbf{L}}_1 * \mathbf{m}(t), \quad (\text{A4})$$

where $\mathbf{h}_1(t)$ is the external perturbation field and $\widehat{\mathbf{L}}_1$ is a certain linear operator, allowing $\mathbf{h}(t)$ to depend on the magnetization distribution. The latter case may describe the influence of the Gilbert damping $-(\alpha/\gamma M_s) \partial \mathbf{M} / \partial t$ through:

$$\widehat{\mathbf{L}}_1 * \mathbf{m} = i \frac{\alpha}{\gamma} \sum_{\nu} \omega_{\nu} (c_{\nu}(t) \mathbf{m}_{\nu}(\mathbf{r}) - \text{c.c.}), \quad (\text{A5})$$

where α is the Gilbert damping constant.

Substituting the series representation Eq. (A3) and the representation of the perturbation field Eq. (A4) into Eq. (A1) and using orthogonality relations Eq. (7), one can obtain the following equations for the SW amplitudes c_{ν} :

$$\frac{dc_{\nu}}{dt} = -i\omega_{\nu} c_{\nu} + i\gamma \sum_{\nu'} \left(S_{\nu, \nu'} c_{\nu'} + S_{\nu, \bar{\nu}'} \bar{c}_{\nu'} \right) + i\gamma h_{\nu}, \quad (\text{A6})$$

where

$$S_{\nu, \nu'} = \frac{\langle \bar{\mathbf{m}}_{\nu} \cdot \widehat{\mathbf{L}}_1 * \mathbf{m}_{\nu'} \rangle - \langle (\hat{\mathbf{u}} \cdot \mathbf{h}_1) (\bar{\mathbf{m}}_{\nu} \cdot \mathbf{m}_{\nu'}) \rangle}{\mathcal{N}_{\nu}}, \quad (\text{A7a})$$

$$S_{\nu, \bar{\nu}'} = \frac{\langle \bar{\mathbf{m}}_{\nu} \cdot \widehat{\mathbf{L}}_1 * \bar{\mathbf{m}}_{\nu'} \rangle - \langle (\hat{\mathbf{u}} \cdot \mathbf{h}_1) (\bar{\mathbf{m}}_{\nu} \cdot \bar{\mathbf{m}}_{\nu'}) \rangle}{\mathcal{N}_{\nu}}, \quad (\text{A7b})$$

$$h_{\nu} = \frac{\langle \bar{\mathbf{m}}_{\nu} \cdot \mathbf{h}_1 \rangle}{\mathcal{N}_{\nu}}. \quad (\text{A7c})$$

In many cases the perturbed equations (A6) can be further simplified by retaining only the diagonal term $S_{\nu,\nu} = i\alpha\omega_\nu \langle \overline{\mathbf{m}}_\nu \cdot \mathbf{m}_\nu \rangle / (\gamma N_\nu)$ (assuming that there are no degenerate modes). The SW damping rate is then given by

$$\Gamma_\nu = \alpha\omega_\nu \frac{\langle \overline{\mathbf{m}}_\nu \cdot \mathbf{m}_\nu \rangle}{N_\nu}. \quad (\text{A8})$$

The damping rate Γ_ν is responsible for the finite linewidth of the resonance peaks, ΔH (FWHM). If the sample is homogeneously magnetized and the precession is circular, the simple relation $\alpha\Delta H = \omega_\nu/\gamma$ holds.

From the equations above, one recovers for the coefficient c_ν the equation of motion of a damped harmonic oscillator:

$$\frac{dc_\nu}{dt} = -i\omega_\nu c_\nu - \Gamma_\nu c_\nu + i\gamma h_\nu. \quad (\text{A9})$$

If a second magnetic layer j' is electrically connected to layer j and spin transfer is allowed between them, the equation of motion must be modified. When a charge current I is flowing through the layers, the additional Slonczewski-Berger term^{6,7} adds to the operator $\widehat{\mathcal{L}}_1$ of Eq. (A4). It is possible to define an effective damping in layer j , which depends on the spin polarized current and on the relative angle between the magnetization in layer j and the direction of the spin polarization $\hat{\mathbf{u}}_{j'}$ ¹⁹:

$$\Gamma_\nu^* = \alpha\omega_\nu \frac{\langle \overline{\mathbf{m}}_\nu \cdot \mathbf{m}_\nu \rangle}{N_\nu} + \frac{I\epsilon}{2eN_s} \frac{\langle (\overline{\mathbf{m}}_\nu \cdot \mathbf{m}_\nu)(\hat{\mathbf{u}}_j \cdot \hat{\mathbf{u}}_{j'}) \rangle}{N_\nu}, \quad (\text{A10})$$

where

$$N_s = \frac{M_j V_j}{\gamma \hbar} \quad (\text{A11})$$

is the dimensionless total number of magnons that can be excited inside the volume V_j of layer j . Here, \hbar is the reduced Planck constant, e the modulus of the electron charge and ϵ the spin polarization efficiency of the current. The threshold current for auto-oscillations in layer j corresponds to $\Gamma_\nu^* = 0$, *i.e.*, if $\hat{\mathbf{u}}_j \parallel \hat{\mathbf{u}}_{j'}$, $I_{\text{th}} = -2\alpha\omega_\nu N_s e/\epsilon$. Using $\epsilon = 0.3$ and the parameters of our thin layer, one can estimate $I_{\text{th}} \simeq -4.8$ mA for the uniform SW mode at 8.1 GHz, in agreement with the experimental data⁸⁸. This result is also in quantitative agreement with calculations performed for our nano-pillar device with no adjusting parameters in the framework of continuous random matrix theory (CRMT) described in Ref.⁸⁹.

We now turn to the periodic external excitation $\mathbf{h}_1(t) = \mathbf{h}_1 \exp^{i\omega t}$, whose amplitude \mathbf{h}_1 is composed of three different contributions,

$$\mathbf{h}_1 = \mathbf{h}_u + \mathbf{h}_{\text{Oe}} + \mathbf{h}_{\text{ST}}, \quad (\text{A12})$$

that we shall detail below.

The first type of excitation corresponds to a uniform RF magnetic field applied perpendicularly to the effective

field \mathbf{H} . This configuration corresponds to conventional FMR spectroscopy. Assuming that the sample is uniformly magnetized along the nano-pillar symmetry axis $\hat{\mathbf{z}}$, it reduces to:

$$\mathbf{h}_u = h_{\text{rf}} \hat{\mathbf{x}}, \quad (\text{A13})$$

where $\hat{\mathbf{x}}$ is a unit vector in the in-plane direction and h_{rf} the linearly polarized amplitude.

SW spectroscopy can also be performed by injecting a uniform RF charge current i_{rf} through the nano-pillar (*i.e.*, along $\hat{\mathbf{z}}$). First, this produces an orthoradial RF Oersted field:

$$\mathbf{h}_{\text{Oe}} = \left[\frac{4\pi}{10} \right] \frac{i_{\text{rf}} \rho}{2\pi R R} (-\sin \phi \hat{\mathbf{x}} + \cos \phi \hat{\mathbf{y}}), \quad (\text{A14})$$

where R is the radius of the nano-pillar and (ρ, ϕ) are the polar coordinates. In this formula, the current should be expressed in A and the prefactor between the square brackets converts A/cm into Oe (cgs units). The maximum amplitude of the RF Oersted field is reached at the periphery of the nano-pillar, $\rho = R$, and equals 1.6 Oe for a peak amplitude $i_{\text{rf}} = 100$ μA and the experimental parameters.

Second, the RF current produces a ST-FMR excitation:

$$\mathbf{h}_{\text{ST}} = \frac{i_{\text{rf}}}{2\pi\lambda} [\hat{\mathbf{u}}_j \times \hat{\mathbf{u}}_{j'}]. \quad (\text{A15})$$

where we have rewritten the spin-transfer efficiency of the charge current in Eq. (A10) as a function of

$$2\pi\lambda = \gamma \frac{2eN_s}{\epsilon}, \quad (\text{A16})$$

which has the dimension of a distance ($\lambda \simeq 200$ nm for our thin layer). If the thin and thick layers are misaligned by an angle β in the plane (y,z) , Eq. (A15) reduces to $\mathbf{h}_{\text{ST}} = i_{\text{rf}}/(2\pi\lambda) \sin \beta \hat{\mathbf{x}}$, which demonstrates that the ST-FMR excitation is equivalent to a linearly polarized RF magnetic field, Eq. (A13). The ST-FMR excitation vanishes if the magnetic layers are parallel. The amplitude ratio between the ST-FMR and the RF Oersted field excitations, both produced by the RF current flowing through the nano-pillar, is $h_{\text{ST}}/h_{\text{Oe}} \simeq (R/\lambda) \sin \beta$. In our geometry, $\lambda \approx 2R$, but due to the small angle β between the layers, the RF Oersted field contribution is much larger than the ST-FMR one. We note that even if $\beta \approx \pi/2$, the contribution of the RF Oersted field cannot be disregarded in general in ST-FMR experiments.

2. Numerical application

In this section, we derive a practical guideline to calculate the eigen-frequencies ω using the analytical formalism developed in section IV A. Let \mathbf{m}_ν be a certain orthogonal basis in the space of the vector functions \mathbf{m} satisfying both the local orthogonality to $\hat{\mathbf{u}}$ and the total

pinning condition at the boundary of the magnetic body. Spin-wave eigen modes can thus be expressed as a series expansion on the \mathbf{m}_ν basis (cf. Eq. (A3)). A general expression for the eigen-frequencies can be found from the condition of vanishing determinant:

$$\left\| \mathcal{N}_{\nu',\nu}\omega - \mathcal{N}_{\nu',\nu} \{ \widehat{\Omega} \}_{\nu',\nu} \right\| = 0, \quad (\text{A17})$$

where for the simplicity of the discussion, it is convenient to introduce a curly bracket notation, to indicate that the enclosed quantity is spatially weighted by the spatial pattern of the mode profile and averaged:

$$\{ \widehat{\Omega} \}_{\nu',\nu} \equiv \frac{\langle \overline{\mathbf{m}}_{\nu'} \cdot \widehat{\Omega} * \mathbf{m}_\nu \rangle}{\mathcal{N}_{\nu',\nu}}, \quad (\text{A18})$$

This echoes the chevron bracket notation introduced in Eq. (1) to indicate the homogeneous spatial average over the volume of the magnetic body. Here \mathcal{N} represents a renormalization quantity, defined by

$$\mathcal{N}_{\nu',\nu} \equiv i \langle \overline{\mathbf{m}}_{\nu'} \cdot (\hat{\mathbf{u}} \times \mathbf{m}_\nu) \rangle, \quad (\text{A19})$$

which has in general off-diagonal elements.

In the case of perpendicularly magnetized disks, where the set of Bessel functions $\frac{1}{2}(\hat{\mathbf{x}} + i\hat{\mathbf{y}})e^{-i\ell\phi}J_\ell(k_{\ell,n}\rho)$ diagonalizes the uncoupled Hamiltonian, the secular Eq. (A17) becomes diagonal and we recover Eq. (8):

$$\omega_\nu = \{ \widehat{\Omega} \}_{\nu,\nu} \quad (\text{A20})$$

We shall now perform the numerical application of the eigen-value of the lowest energy mode ($\ell, n = 0, 0$) using the parameters of our nano-pillar shown in Table I. We will drop the subscript ν to the curly brackets, understanding that the spatial average in Eq. (A20) is made over the uniform mode $\mathbf{m}_\nu = \frac{1}{2}J_0(k_0\rho)(\hat{\mathbf{x}} + i\hat{\mathbf{y}})$, where $k_0 = 2.4048/R$ is its wave-vector. In this case the value of the normalization constant is simply $\mathcal{N}_0 = \langle J_0^2 \rangle = J_1^2(k_0R) = 0.2695$.

The different contributions that enter inside the operator $\{ \widehat{\Omega} \}$ are detailed in Eq. (4):

$$\{ \widehat{\Omega} \} = \gamma \{ H \} + 4\pi\gamma M_j \{ \widehat{\mathbf{G}} \}. \quad (\text{A21})$$

We start with the calculation of the amplitude of effective magnetic field, the first term on the right hand side of Eq. (A21). As shown by Eq. (5), the scalar value H along $\hat{\mathbf{z}}$ decomposes itself in two terms:

$$\{ H \} = \{ \hat{\mathbf{z}} \cdot \mathbf{H}_0 \} - 4\pi M_s \{ \hat{\mathbf{z}} \cdot \widehat{\mathbf{G}} * \hat{\mathbf{z}} \}. \quad (\text{A22})$$

The term $\hat{\mathbf{z}} \cdot \widehat{\mathbf{G}} * \hat{\mathbf{z}}$ represents the static magnetic self-interaction. In the case of homogeneously magnetized body, the inhomogeneous exchange contribution to the static self-interaction is strictly null and the second term of Eq. (A22) reduces to the magneto-dipolar contribution $\widehat{\mathbf{G}}^{(d)}$, which has the following form in the wave-vector representation:

$$\widehat{\mathbf{G}}^{(d)}(\mathbf{r}) = \int D(\mathbf{k}) \frac{\mathbf{k} \otimes \mathbf{k}}{k^2} \exp^{i\mathbf{k} \cdot \mathbf{r}} d^3\mathbf{k}, \quad (\text{A23})$$

where $D(\mathbf{k})$ is the Fourier transform of the body shape function⁹⁰ and the symbol \otimes denotes direct product of vectors. For a disk of radius R and thickness t , an analytical expression for the different position-dependent demagnetization tensor elements of a disk $N_{uv}[\mathbf{r},t](\mathbf{r}) \equiv \hat{\mathbf{u}}(\mathbf{r}) \cdot \widehat{\mathbf{G}}^{(d)} * \hat{\mathbf{v}}$ valid in the whole space are available in Ref.⁹¹. For perpendicularly magnetized disks where $\hat{\mathbf{u}} = \hat{\mathbf{v}} = \hat{\mathbf{z}}$, the expression of the self-integral becomes

$$\{ N_{zz}^{(j,j)} \} = \frac{1}{\langle J_0^2 \rangle} \int_{V_j} d^2\rho dz J_0^2(k_0\rho) N_{zz}[\mathbf{r},t_j](\rho, z), \quad (\text{A24})$$

for both the thin ($j = a$) and thick ($j = b$) layers. Their numerical values are displayed in Table. III.

The term $\{ \hat{\mathbf{z}} \cdot \mathbf{H}_0 \}$ of Eq. (A22) is the projection on the precession axis of the total applied magnetic field. It comprises the external magnetic field $\{ H_{\text{ext}} \} = H_{\text{ext}}$, the stray field of the mechanical-FMR probe $\{ H_{\text{sph}} \} = 190$ Oe and the cross-magneto-dipolar static interactions between each layer. The latter can be estimated from the cross tensor elements of the static magneto-dipolar field of the j' -th disk produced over the volume of the j -th disks:

$$\{ N_{zz}^{(j,j')} \} = \frac{1}{\langle J_0^2 \rangle} \int_{V_j} d^2\rho dz J_0^2(k_0\rho) N_{zz}[\mathbf{r},t_{j'}](\rho, z + z_0), \quad (\text{A25})$$

where z_0 is the distance between the centers of the two axially aligned disks. The numerical values of the cross tensor elements are reported in Table. III. Putting all the above elements together, the total effective field simply writes:

$$\{ H \} = H_{\text{ext}} + \{ H_{\text{sph}} \} - 4\pi \{ N_{zz}^{(j,j)} \} M_j - 4\pi \{ N_{zz}^{(j,j')} \} M_{j'}. \quad (\text{A26})$$

We now turn our attention to the integration $4\pi M_j \{ \widehat{\mathbf{G}} \}$, the second term on the right hand side of Eq. (A21). We recall that for Py the operator $\widehat{\mathbf{G}} = \widehat{\mathbf{G}}^{(e)} + \widehat{\mathbf{G}}^{(d)}$ is the sum of the inhomogeneous exchange and magneto-dipolar interactions. In the wave-vector representation, $\widehat{\mathbf{G}}^{(e)} = \Lambda_{\text{ex}}^2 k^2 \widehat{\mathbf{I}}$, where the exchange length $\Lambda_{\text{ex}} = \sqrt{2J/(4\pi M_j^2)}$ depends on the exchange stiffness constant J , expressed in erg/cm ($= 10^{-6}$ in Py). It produces the exchange field:

$$\{ H_{\text{ex}} \} = 4\pi M_j \Lambda_{\text{ex}}^2 k_0^2, \quad (\text{A27})$$

which yields the value $\{ H_{\text{ex}} \} = 110$ Oe.

The other contribution is the dynamic magneto-dipolar self-interaction, which represents the depolarization field of the SW mode on itself. For the $\ell = 0$ modes, an analytical expression can be derived:

$$\{ N_{xx}^{(j,j')} \} = \frac{1}{\langle J_0^2 \rangle} \int_{V_j} d^2\rho dz J_0(k_0\rho) \int_0^R du \frac{\partial N_{xx}[u,t_{j'}](\rho, z)}{\partial u} J_0(k_0u), \quad (\text{A28})$$

where the quantity in the second integral is the magnetic stray field produced at the spatial position \mathbf{r} by a cylindrical tube of width du , radius u , and thickness $t_{j'}$, homogeneously magnetized⁹² along $\hat{\mathbf{x}}$ by $J_0(k_0u)$. We use

the same expression above to write the self- and cross-contribution, understanding implicitly that the spacer value z_0 should be added in the later case, as shown in Eq. (A25). The values of the self- and cross-tensor elements are reported in the last line of Table. III. We mention, that an approximate expression of the self-Eq. (A28) has been derived by Kalinikos and Slavin⁹³ for the lowest SW branch of platelet shape bodies with uniform magnetization across the film thickness. This expression reduces to

$$\{N_{xx}\} \simeq \frac{1}{2} (1 - G_0^\perp) \quad (\text{A29})$$

where the analytical expression of $G_{\ell,n}^\perp$ for Bessel functions is given by Eq. (26) in ref³⁸.

The cross elements are responsible for the dynamic dipolar coupling detailed in section IV B.

$$h_{j,j'} = 4\pi \{N_{xx}^{(j,j')}\} M_{j'} \quad (\text{A30})$$

The value of the coupling frequency Ω for the lowest energy mode yields:

$$\Omega \simeq \gamma \sqrt{\{N_{xx}^{(a,b)}\} 4\pi M_b \{N_{xx}^{(b,a)}\} 4\pi M_a}, \quad (\text{A31})$$

which leads to $\Omega/2\pi \simeq 0.56$ GHz.

Neglecting the dynamical dipolar coupling (the generalization to $\Omega \neq 0$ is Eq. (15)), we derive an expression for the eigen-value of index $\nu = j_{0,0}$:

$$\frac{\omega_\nu}{\gamma} = \{H\} + 4\pi \{N_{xx}^{(j,j)}\} M_j + \{H_{\text{ex}}\}, \quad (\text{A32})$$

$j = a, b$ being the layer index and $\{H\}$ being defined in Eq. (A26). Eq. (A32) is a simplified expression valid for circularly polarized modes ($\ell = 0$ index), where we have taken advantage of the equality $\{N_{xx}\}_0 = \{N_{yy}\}_0$ in our circular disk. This expression can be extended to higher order modes by using $\{N_{xx}\}_{\ell,n} \approx \{N_{xx}\}_0 \sqrt{k_{\ell,n}/k_0}$ inside Eq. (A32). This approximation is derived from the ellipticity of $\ell \neq 0$ modes ($\{N_{xx}\} \neq \{N_{yy}\}$). One needs thus two separate equations (A32) for the values of ω for each cartesian axis³⁸: one proportional to $m_x^2/(m_x m_y)$, the other to $m_y^2/(m_x m_y)$. The product of these two equations is independent of the ellipticity, leading to the general expression for the eigen-value of arbitrary index $\nu = j_{\ell,n}$:

$$\frac{\omega_\nu^2}{\gamma^2} = (\{H\}_\nu + 4\pi \{N_{xx}^{(j,j)}\}_\nu M_j + \{H_{\text{ex}}\}_\nu) \times (\{H\}_\nu + 4\pi \{N_{yy}^{(j,j)}\}_\nu M_j + \{H_{\text{ex}}\}_\nu), \quad (\text{A33})$$

which can be seen as a generalization of the Kittel formula for arbitrary shaped multi-body.

Equating $H_{a_{00}} = H_{\otimes}$ and $H_{b_{00}} = H_{\ominus}$ in Eq. (A32), where $H_{a_{00}}$ and $H_{b_{00}}$ are the resonance fields at $f_{\text{fix}} = 8.1$ GHz of the uniform modes in the thin and thick disks, respectively, leads to $4\pi M_a = 8.0 \times 10^3$ G and $4\pi M_b = 9.6 \times 10^3$ G.

TABLE III. Values of the self- and cross- depolarization tensor elements weighted by the precession profile of the uniform mode for the thin ($j = a$) and thick ($j = b$) disks.

	(a, a)	(a, b)	(b, a)	(b, b)
$\{N_{zz}^{(j,j')}\}$	+0.979	-0.068	-0.017	+0.919
$\{N_{xx}^{(j,j')}\}$	+0.016	+0.042	+0.011	+0.056

Finally, the above formalism also enables to determine the angle $\theta_j = (\hat{z}, \hat{u}_j)$ between the equilibrium direction of the magnetization in layer j and the normal axis when the bias field is applied at a polar angle $\theta_H = (\hat{z}, \mathbf{H}_{\text{ext}})$. From the equality $\hat{u} \times \mathbf{H}_{\text{ext}} = 4\pi M_j \hat{u} \times \langle \mathbf{G}^{(d_j)} \rangle \hat{u}$, one extracts the relationship:

$$H_{\text{ext}} \sin(\theta_j - \theta_H) = 2\pi M_j (\{N_{zz}^{(jj)}\} - \{N_{xx}^{(jj)}\}) \sin 2\theta_j \quad (\text{A34})$$

The angle θ_j is useful to estimate the shift to lower field of the FMR spectrum³⁸, $2\pi M_j (\{N_{zz}^{(j)}\} - \{N_{xx}^{(j)}\}) (1 - \cos 2\theta_j) \approx 420$ Oe, when $\theta_b = 13^\circ$ in the thick layer.

Appendix B: Methods and calibration

1. Mechanical vibration amplitude

Here, we detail the experimental protocol used to calibrate the amplitudes of the uniform RF magnetic field and of the mechanical-FMR signal. The procedure uses the non-linear properties of the magnetization dynamics and consists in studying the power dependence of the line shape. In the following, ΔH denotes the FWHM linewidth measured in the linear regime.

We use the onset of foldover as a mean to calibrate the strength of the RF field produced by the microwave antenna. This non-linear effect is responsible for the asymmetric shape of the resonance peaks in FIGS. 2 and 3. In fact, it was pointed out by Anderson and Suhl⁵¹ that the resonance curve at high power should be skewed, due to the static change of the magnetization M_z , which also shifts the resonance frequency. For a normally magnetized sample, this non-linear frequency shift is positive (blue-shift), and the field-sweep line shapes are distorted towards low field. There is a critical strength of the RF magnetic field h_c (linearly polarized amplitude) for which the slope of the resonance curve becomes infinite on the low field side of the resonance⁵²:

$$h_c = 2\Delta H \sqrt{\frac{2\Delta H}{3\sqrt{3} |\{N_{zz}\} - \{N_{xx}\}| 4\pi M_s}} \quad (\text{B1})$$

where $\{N_{zz}\} - \{N_{xx}\}$ is the difference between the depolarization factors in the longitudinal and transverse directions. Experimentally we find that for the peak at H_{\ominus} , this onset is reached when the output power of the synthesizer at 8.1 GHz is $P_0 = +9$ dBm. Using the

magnetic properties of the thick layer (Table I), we infer from Eq. (B1) that at the critical onset of foldover, the strength of the RF magnetic field is $h_c = 4.2 \pm 0.8$ Oe. We note, that this value is in agreement with the estimation made by directly evaluating the field produced by the RF current flowing in the antenna at 8.1 GHz for this output power, $h_{\text{rf}} = 5.5 \pm 1$ Oe.

Furthermore, this procedure gives a calibration of the amplitude of the mechanical-FMR signal $\langle \Delta M_z \rangle$. At the onset of foldover, the longitudinal change of the magnetization is indeed⁵¹

$$4\pi \langle \Delta M_z \rangle = \frac{4}{3\sqrt{3}} \Delta H. \quad (\text{B2})$$

A numerical application of Eq. (B2) yields $4\pi \langle \Delta M_z \rangle = 36 \pm 4$ G, which corresponds to the critical angle of precession $\langle \theta_c \rangle = 5^\circ$. We have used this calibration of the cantilever vibration amplitude to evaluate the change of the longitudinal magnetization at the maximum of the peak at H_0 in FIG. 2a.

2. Microwave setup

In this appendix, we give some details on the microwave circuit, which was carefully design to minimize the cross-talk between the RF field and RF current excitation parts.

The calibration of the RF magnetic field produced by the microwave antenna has been presented in the previous appendix. In order to calibrate the RF current flowing through the nano-pillar with respect to the synthesizer output power injected into the contact electrodes, we have first used a standard microwave setup. The nano-pillar electrodes are directly connected to the microwave synthesizer through a picoprobe, a bias-T, and a semi-rigid coaxial line, that allow to perform voltage-FMR spectroscopy. In this experiment, the amplitude of i_{rf} flowing through the nano-pillar can be accurately determined, owing to the determination of losses and reflexions in the microwave circuit using a network analyzer. Then, the same experiment is repeated inside the MRFM setup, in which the contact electrodes are wire bounded to a microwave cable and the circuit contains more connections. The comparison with the standard setup yields an estimation of the rms amplitude of the RF current in the mechanical-FMR setup: $i_{\text{rf}} = 170 \pm 40$ μA for an output power of -22 dBm injected at 8.1 GHz through the contact electrodes.

It is also possible to estimate experimentally the high frequency coupling between the microwave antenna and the electrodes that contact the nano-pillar. For this, we exploit the fact that in the exact perpendicular configuration, different SW modes are excited by the uniform RF field ($\ell = 0$ -index) and by the RF current ($\ell = +1$ -index). If the RF magnetic field used to excite the conventional FMR spectrum would induce any relevant RF eddy current through the nano-pillar, $\ell = +1$ modes which are

excited in the SW spectrum of FIG. 2b should also be detected in the SW spectrum of FIG. 2a, which is not the case. We deduce from this observation that for an output power of $+3$ dBm injected in the antenna, the induced eddy current through the nano-pillar is less than when injecting -38 dBm directly through the contact electrodes, *i.e.*, $i_{\text{rf}} < 30$ μA . So, at $f_{\text{fix}} = 8.1$ GHz, the isolation between the two parts of the microwave circuit is better than 40 dB. However, we note that the latter depends on the frequency, and that for some particular values, it can drop to only 20 dB.

Still, owing to the broadband design of the contact electrodes and to the low microwave power required to excite SW modes with the RF current excitation part, it is possible to acquire FMR spectra at a fixed bias magnetic field H_{fix} by sweeping the frequency of the RF current. We mention that in the frequency-sweep experiments presented in FIG. 4a, the output power of the synthesizer is kept at -22 dBm over the full frequency range (4 to 18 GHz), which results in an amplitude variation of i_{rf} , mainly associated to frequency dependent losses in the circuit. We also note that the same frequency-sweep experiment cannot be performed as cleanly with the RF field excitation due to the high power that has to be injected in the microwave antenna and to the dependence of the isolation on frequency mentioned above.

3. Cavity-FMR characterization of the extended film

Before the nano-fabrication of the nano-pillar devices, a reference film of Cu60 | Py_b15 | Cu10 | Py_a4 | Au25 (thicknesses in nm) is cut out from the Si wafer for characterization purpose. The extraction of the material parameters is obtained independently on this reference film by a reflexion X-band spectrometer (9.6 GHz) operating at room temperature. The experiment consists in measuring the resonance spectra of the multi-layer as a function of the polar angle θ_H between the applied field and the normal to the film. The resonance field of the layer $j = a, b$ as a function of θ_H depends only on the gyromagnetic ratio γ and on the total perpendicular anisotropy field, which here reflects entirely the demagnetizing field $4\pi M_j$ of the layer⁹⁴. The obtained values for the gyromagnetic ratio (identical for both layers) and the magnetizations are collected in Table I. The magnetization of the thick layer (9.6 kOe) corresponds to the expected value for bulk Py with composition Ni₈₀Fe₂₀. The magnetization of the thin layer is 1.4 kG smaller, which reflects the reduction of the magnetization in the interfacial layer (of the order of 1 nm), due to the gradual composition variation of the NiFe alloy from Ni₈₀Fe₂₀ to the normal metal (Cu or Au)^{58,60}.

An estimate of the damping parameter and the amount of inhomogeneous broadening can also be obtained from the angular dependence of the linewidth of the resonant mode associated to each layer. The linewidth is in gen-

eral the sum of two contributions: an intrinsic relaxation of the magnetization vector (homogeneous width) and an inhomogeneous broadening corresponding to a distribution of resonance fields (whose main sources have been described for a Permalloy polycrystalline layer⁹⁴). The intrinsic damping parameter is deduced from the parallel geometry linewidth. In the Py_b 15 nm thick layer, the linewidths observed in the parallel and perpendicular geometries are respectively: $\Delta H_{\parallel b} = 64$ Oe and $\Delta H_{\perp b} = 73$ Oe. The higher value observed in the perpendicular geometry reveals a fair amount of inhomogeneities⁹⁴. The linewidth observed in the parallel geometry corresponds to an intrinsic damping parameter $\alpha_b = (0.9 \pm 0.1) \times 10^{-2}$. For the thin Py_a 4 nm layer,

$\Delta H_{\parallel a} = 83$ Oe and $\Delta H_{\perp a} = 171$ Oe. From the parallel geometry linewidth, we deduce an intrinsic damping parameter $\alpha_a = (1.5 \pm 0.3) \times 10^{-2}$. This value is higher than for the thick layer because of the larger effect of the diffusion of the microwave magnetization of the conduction electrons in the adjacent normal metal layers⁶⁰, associated to the fact that the thin layer thickness (4 nm) is less than the spin-diffusion length in Py. The much larger value $\Delta H_{\perp a}$ is associated to a large contribution of the inhomogeneous broadening arising from a substantial effect of interfacial roughness (and dispersion of heights of the crystallites of the base) on the thin Py layer grown on top of a 85 nm thick metallic base.

* Main co-author: gregoire.deloubens@cea.fr

† Principal investigator and main co-author: oklein@cea.fr

- ¹ S. Wolf, D. D. Awschalom, R. A. Buhrman, J. Daughton, S. von Molnar, M. L. Roukes, A. Y. Chtchelkanova, and D. M. Treger, *Science* **294**, 1488 (2001).
- ² M. N. Baibich, J. M. Broto, A. Fert, F. N. V. Dau, F. Petroff, P. Etienne, G. Creuzet, A. Friederich, and J. Chazelas, *Phys. Rev. Lett.* **61**, 2472 (1988).
- ³ G. Binasch, P. Grunberg, F. Saurenbach, and W. Zinn, *Phys. Rev. B* **39**, 4828 (1989).
- ⁴ B. Dieny, V. Speriosu, B. Gurney, S. Parkin, D. Wilhoit, K. Roche, S. Metin, D. Peterson, and S. Nadimi, *J. Magn. Magn. Mater.* **93**, 101 (1991).
- ⁵ M. Pannetier, C. Fermon, G. L. Goff, J. Simola, and E. Kerr, *Science* **304**, 1648 (2004).
- ⁶ J. Slonczewski, *J. Magn. Magn. Mater.* **159**, L1 (1996).
- ⁷ L. Berger, *Phys. Rev. B* **54**, 9353 (1996).
- ⁸ M. Tsoi, A. G. M. Jansen, J. Bass, W.-C. Chiang, M. Seck, V. Tsoi, and P. Wyder, *Phys. Rev. Lett.* **80**, 4281 (1998).
- ⁹ F. J. Albert, J. A. Katine, R. A. Buhrman, and D. C. Ralph, *Appl. Phys. Lett.* **77**, 3809 (2000).
- ¹⁰ J. Grollier, V. Cros, A. Hamzis, J. M. George, H. Jaffres, A. Fert, G. Faini, J. Ben Youssef, and H. Legall, *Appl. Phys. Lett.* **78**, 3663 (2001).
- ¹¹ S. I. Kiselev, J. C. Sankey, I. N. Krivorotov, N. C. Emley, R. J. Schoelkopf, R. A. Buhrman, and D. C. Ralph, *Nature* **425**, 380 (2003).
- ¹² W. H. Rippard, M. R. Pufall, S. Kaka, S. E. Russek, and T. J. Silva, *Phys. Rev. Lett.* **92**, 027201 (2004).
- ¹³ V. E. Demidov, S. O. Demokritov, B. Hillebrands, M. Laufenberg, and P. P. Freitas, *Appl. Phys. Lett.* **85**, 2866 (2004).
- ¹⁴ G. Woltersdorf, O. Mosendz, B. Heinrich, and C. H. Back, *Phys. Rev. Lett.* **99**, 246603 (2007).
- ¹⁵ G. de Loubens, V. V. Naletov, O. Klein, J. Ben Youssef, F. Boust, and N. Vukadinovic, *Phys. Rev. Lett.* **98**, 127601 (2007).
- ¹⁶ G. de Loubens, V. V. Naletov, M. Viret, O. Klein, H. Hurdequint, J. Ben Youssef, F. Boust, and N. Vukadinovic, *J. Appl. Phys.* **101**, 09F514 (2007).
- ¹⁷ G. Gubbiotti, M. Madami, S. Tacchi, G. Carlotti, H. Tanigawa, and T. Ono, *J. Phys. D: Appl. Phys.* **41**, 134023 (2008).
- ¹⁸ P. S. Keatley, V. V. Kruglyak, A. Neudert, E. A. Galaktionov, R. J. Hicken, J. R. Childress, and J. A. Katine, *Phys. Rev. B* **78**, 214412 (2008).
- ¹⁹ A. Slavin and V. Tiberkevich, *IEEE Trans. Magn.* **45**, 1875 (2009).
- ²⁰ A. V. Nazarov, H. S. Cho, J. Nowak, S. Stokes, and N. Tabat, *Appl. Phys. Lett.* **81**, 4559 (2002).
- ²¹ N. Stutzke, S. L. Burkett, and S. E. Russek, *Appl. Phys. Lett.* **82**, 91 (2003).
- ²² S. Petit, C. Baraduc, C. Thirion, U. Ebels, Y. Liu, M. Li, P. Wang, and B. Dieny, *Phys. Rev. Lett.* **98**, 077203 (2007).
- ²³ A. Helmer, S. Cornelissen, T. Devolder, J.-V. Kim, W. van Roy, L. Lagae, and C. Chappert, *Phys. Rev. B* **81**, 094416 (2010).
- ²⁴ A. A. Tulapurkar, Y. Suzuki, A. Fukushima, H. Kubota, H. Maehara, K. Tsunekawa, D. D. Djayaprawira, N. Watanabe, and S. Yuasa, *Nature* **438**, 339 (2005).
- ²⁵ J. C. Sankey, P. M. Braganca, A. G. F. Garcia, I. N. Krivorotov, R. A. Buhrman, and D. C. Ralph, *Phys. Rev. Lett.* **96**, 227601 (2006).
- ²⁶ W. Chen, J.-M. L. Beaujour, G. de Loubens, A. D. Kent, and J. Z. Sun, *Appl. Phys. Lett.* **92**, 012507 (2008).
- ²⁷ W. Chen, G. de Loubens, J.-M. L. Beaujour, A. D. Kent, and J. Z. Sun, *J. Appl. Phys.* **103**, 07A502 (2008).
- ²⁸ N. Biziere, E. Murè, and J.-P. Ansermet, *Phys. Rev. B* **79**, 012404 (2009).
- ²⁹ C. T. Boone, J. A. Katine, J. R. Childress, V. Tiberkevich, A. Slavin, J. Zhu, X. Cheng, and I. N. Krivorotov, *Phys. Rev. Lett.* **103**, 167601 (2009).
- ³⁰ W. H. Rippard, A. M. Deac, M. R. Pufall, J. M. Shaw, M. W. Keller, S. E. Russek, G. E. W. Bauer, and C. Serpico, *Phys. Rev. B* **81**, 014426 (2010).
- ³¹ N. Biziere and C. Fermon, *Appl. Phys. Lett.* **92**, 092503 (2008).
- ³² N. Biziere and C. Fermon, *Phys. Rev. B* **78**, 064408 (2008).
- ³³ D. Houssameddine, U. Ebels, B. Delaët, B. Rodmacq, I. Firastrau, F. Ponthenier, M. Brunet, C. Thirion, J.-P. Michel, L. Prejbeanu-Buda, M.-C. Cyrille, O. Redon, and B. Dieny, *Nature Mater.* **6**, 447 (2007).
- ³⁴ Z. Zhang, P. C. Hammel, and P. E. Wigen, *Appl. Phys. Lett.* **68**, 2005 (1996).
- ³⁵ K. Wago, D. Botkin, C. S. Yannoni, and D. Rugar, *Appl. Phys. Lett.* **72**, 2757 (1998).
- ³⁶ A. Jander, J. Moreland, and P. Kabos, *J. Appl. Phys.* **89**, 7086 (2001).

- ³⁷ V. Charbois, V. V. Naletov, J. Ben Youssef, and O. Klein, *J. Appl. Phys.* **91**, 7337 (2002).
- ³⁸ O. Klein, G. de Loubens, V. V. Naletov, F. Boust, T. Guillet, H. Hurdequint, A. Leksikov, A. N. Slavin, V. S. Tiberkevich, and N. Vukadinovic, *Phys. Rev. B* **78**, 144410 (2008).
- ³⁹ G. de Loubens, V. V. Naletov, and O. Klein, *Phys. Rev. B* **71**, 180411 (2005).
- ⁴⁰ V. V. Naletov, G. de Loubens, V. Charbois, O. Klein, V. S. Tiberkevich, and A. N. Slavin, *Phys. Rev. B* **75**, 140405 (2007).
- ⁴¹ G. de Loubens, A. Riegler, B. Pigeau, F. Lochner, F. Boust, K. Y. Guslienko, H. Hurdequint, L. W. Molenkamp, G. Schmidt, A. N. Slavin, V. S. Tiberkevich, N. Vukadinovic, and O. Klein, *Phys. Rev. Lett.* **102**, 177602 (2009).
- ⁴² B. Pigeau, G. de Loubens, O. Klein, A. Riegler, F. Lochner, G. Schmidt, L. W. Molenkamp, V. S. Tiberkevich, and A. N. Slavin, *Appl. Phys. Lett.* **96**, 132506 (2010).
- ⁴³ B. Pigeau, G. de Loubens, O. Klein, A. Riegler, F. Lochner, G. Schmidt, and L. W. Molenkamp, *Nature Phys.* **7**, 26 (2011).
- ⁴⁴ We mention here that the measured amplitude of the GMR effect in our sample is $\Delta R_{\text{GMR}} = 25 \text{ m}\Omega$, in agreement with the value calculated by CRMT for the multi-layer stack composition⁸⁹.
- ⁴⁵ O. Klein, V. Charbois, V. V. Naletov, and C. Fermon, *Phys. Rev. B* **67**, 220407(R) (2003).
- ⁴⁶ O. Klein, V. Charbois, V. V. Naletov, and C. Fermon, *J. Magn. Magn. Mater.* **272**, E1027 (2004).
- ⁴⁷ I. Lee, Y. Obukhov, G. Xiang, A. Hauser, F. Yang, P. Banerjee, D. Pelekhov, and P. Hammel, *Nature* **466**, 845 (2010).
- ⁴⁸ V. Charbois, V. V. Naletov, J. Ben Youssef, and O. Klein, *Appl. Phys. Lett.* **80**, 4795 (2002).
- ⁴⁹ V. V. Naletov, V. Charbois, O. Klein, and C. Fermon, *Appl. Phys. Lett.* **83**, 3132 (2003).
- ⁵⁰ R. E. Arias and D. L. Mills, *Phys. Rev. B* **79**, 144404 (2009).
- ⁵¹ P. W. Anderson and H. Suhl, *Phys. Rev.* **100**, 1788 (1955).
- ⁵² E. Schlömann, *Ferromagnetic resonance at high power levels*, Tech. Rep. (Technical Report No. R-48, 1959) (unpublished).
- ⁵³ W. Chen, G. de Loubens, J.-M. L. Beaujour, J. Z. Sun, and A. D. Kent, *Appl. Phys. Lett.* **95**, 172513 (2009).
- ⁵⁴ Y. Tserkovnyak, A. Brataas, G. E. W. Bauer, and B. I. Halperin, *Rev. Mod. Phys.* **77**, 1375 (2005).
- ⁵⁵ M. V. Costache, M. Sladkov, S. M. Watts, C. H. van der Wal, and B. J. van Wees, *Phys. Rev. Lett.* **97**, 216603 (2006).
- ⁵⁶ J. N. Kupferschmidt, S. Adam, and P. W. Brouwer, *Phys. Rev. B* **74**, 134416 (2006).
- ⁵⁷ As expected, this value corresponds to the stray field of the magnetic sphere with magnetic moment $m = 2 \times 10^{-10} \text{ emu}$ set at a distance $s = 1.3 \text{ }\mu\text{m}$ from the nano-pillar.
- ⁵⁸ S. Mizukami, Y. Ando, and T. Miyazaki, *Jpn J. Appl. Phys.* **40**, 580 (2001).
- ⁵⁹ J.-M. L. Beaujour, J. H. Lee, A. D. Kent, K. Krycka, and C.-C. Kao, *Phys. Rev. B* **74**, 214405 (2006).
- ⁶⁰ H. Hurdequint, *J. Magn. Magn. Mater.* **310**, 2061 (2007).
- ⁶¹ A. G. Gurevich and G. A. Melkov, *Magnetization Oscillations and Waves* (CRC Press, 1996).
- ⁶² M. Bailleul, R. Hollinger, and C. Fermon, *Phys. Rev. B* **73**, 104424 (2006).
- ⁶³ K. Y. Guslienko, S. O. Demokritov, B. Hillebrands, and A. N. Slavin, *Phys. Rev. B* **66**, 132402 (2002).
- ⁶⁴ It will lead to an error of the order of $4\pi\gamma M_s(t/R)^2$ in the frequency, which is much smaller than, *e.g.*, the distance between different modes.
- ⁶⁵ J. F. Dillon, *J. Appl. Phys.* **31**, 1605 (1960).
- ⁶⁶ R. W. Damon and J. R. Eshbach, *J. Phys. Chem. Solids* **19**, 308 (1961).
- ⁶⁷ C. Kittel, *Phys. Rev.* **110**, 1295 (1958).
- ⁶⁸ M. Belmeguenai, T. Martin, G. Woltersdorf, M. Maier, and G. Bayreuther, *Phys. Rev. B* **76**, 104414 (2007).
- ⁶⁹ G. Gubbiotti, M. Kostylev, N. Sergeeva, M. Conti, G. Carlotti, T. Ono, A. N. Slavin, and A. Stashkevich, *Phys. Rev. B* **70**, 224422 (2004).
- ⁷⁰ J. Ben Youssef and A. Layadi, *J. Appl. Phys.* **108**, 053913 (2010).
- ⁷¹ O. Myttriiev, T. Meitzler, E. Bankowski, A. Slavin, and V. Tiberkevich, *J. Phys.: Condens. Matter* **22**, 136001 (2010).
- ⁷² http://www.insilicio.fr/pdf/Spinflow_3D.pdf.
- ⁷³ W. E and X.-P. Wang, *SIAM J. Numer. Anal.* **38**, 1647 (2001).
- ⁷⁴ M. d'Aquino, C. Serpico, G. Miano, and C. Forestiere, *J. Comput. Phys.* **228**, 6130 (2009).
- ⁷⁵ R. Lehoucq, D. Sorensen, and C. Yang, *ARPACK Users' Guide: Solution of Large-Scale Eigenvalue Problems with Implicitly Restarted Arnoldi Methods* (SIAM Publications, Philadelphia, 1998).
- ⁷⁶ R. D. McMichael and M. D. Stiles, *J. Appl. Phys.* **97**, 10J901 (2005).
- ⁷⁷ The two images of FIGS. 11b and 11c are top and bottom view of the nano-pillar, hence one of them should be mirrored for direct comparison of the relative phase between the layers.
- ⁷⁸ M. P. Kostylev, A. A. Stashkevich, N. A. Sergeeva, and Y. Roussigné, *J. Magn. Magn. Mater.* **278**, 397 (2004).
- ⁷⁹ B. Pigeau et al., in preparation.
- ⁸⁰ S. Kaka, M. R. Pufall, W. H. Rippard, T. J. Silva, S. E. Russek, and J. A. Katine, *Nature* **437**, 389 (2005).
- ⁸¹ F. B. Mancoff, N. D. Rizzo, B. N. Engel, and S. Tehrani, *Nature* **437**, 393 (2005).
- ⁸² A. N. Slavin and V. S. Tiberkevich, *Phys. Rev. B* **72**, 092407 (2005).
- ⁸³ J. Grollier, V. Cros, and A. Fert, *Phys. Rev. B* **73**, 060409 (2006).
- ⁸⁴ B. Georges, J. Grollier, M. Darques, V. Cros, C. Deranlot, B. Marcilhac, G. Faini, and A. Fert, *Phys. Rev. Lett.* **101**, 017201 (2008).
- ⁸⁵ A. Ruotolo, V. Cros, B. Georges, A. Dussaux, J. Grollier, C. Deranlot, R. Guillemet, K. Bouzouhane, S. Fusil, and A. Fert, *Nature Nanotech.* **4**, 528 (2009).
- ⁸⁶ S. Urazhdin, P. Tabor, V. Tiberkevich, and A. Slavin, *Phys. Rev. Lett.* **105**, 104101 (2010).
- ⁸⁷ A. Dussaux, A. V. Khvalkovskiy, J. Grollier, V. Cros, A. Fukushima, M. Konoto, H. Kubota, K. Yakushiji, S. Yuasa, K. Ando, and A. Fert, *Appl. Phys. Lett.* **98**, 132506 (2011).
- ⁸⁸ A. Hamadeh et al., in preparation.
- ⁸⁹ V. S. Rychkov, S. Borlenghi, H. Jaffres, A. Fert, and X. Waintal, *Phys. Rev. Lett.* **103**, 066602 (2009).
- ⁹⁰ M. Beleggia and M. D. Graef, *J. Magn. Magn. Mater.* **263**, L1 (2003).
- ⁹¹ S. Tandon, M. Beleggia, Y. Zhu, and M. De Graef, *J. Magn. Magn. Mater.* **271**, 9 (2004).

⁹² M. Beleggia, S. Tandon, Y. Zhu, and M. D. Graef, *J. Magn. Magn. Mater.* **278**, 270 (2004).

⁹³ B. A. Kalinikos and A. N. Slavin, *J. Phys. C* **19**, 7013 (1986).

⁹⁴ H. Hurdequint, *J. Magn. Magn. Mater.* **242-245**, 521 (2002).